TORC2 dependent phosphorylation modulates calcium regulation of fission yeast myosin.

Karen Baker[1], Irene A. Gyamfi[1], Gregory I. Mashanov[2], Justin E. Molloy[2], Michael A. Geeves[1] and Daniel P. Mulvihill[1,3]

[1] School of Biosciences, University of Kent, Canterbury, Kent, CT2 7NJ, UK.

[2] The Francis Crick Institute, 1 Midland Road, London NW1 1AT, UK

[3] Author for correspondence e-mail: d.p.mulvihill@kent.ac.uk

Tel: +44 (0) 1227 827239

Key words: pombe, endocytosis, calmodulin, Tor kinase.

Running Title: Phosphorylation & calcium co-dependent myosin regulation

Abstract

All cells have the ability to respond to changes in their environment. Signalling networks modulate cytoskeleton and membrane organisation to impact cell cycle progression, polarised cell growth and multicellular development according to the environmental setting. Using diverse *in vitro*, *in vivo* and single molecule techniques we have explored the role of myosin-1 signalling in regulating endocytosis during both mitotic and meiotic cell cycles. We have established that a conserved serine within the neck region of the sole fission yeast myosin-1 is phosphorylated in a TORC2 dependent manner to modulate myosin function. Myo1 neck phosphorylation brings about a change in the conformation of the neck region and modifies its interaction with calmodulins, Myo1 dynamics at endocytic foci, and promotes calcium dependent switching between different calmodulin light chains. These data provide insight into a novel mechanism by which myosin neck phosphorylation modulates acto-myosin dynamics to control polarised cell growth in response to mitotic and meiotic cell-cycle progression and the cellular environment.

Introduction

The actin cytoskeleton underpins cellular organisation by maintaining cell shape and through the transmission of mechanical signals between the cell periphery and nucleus, to influence protein expression, organisation and cellular architecture in response to needs of the cell. Myosins, actin-associated motor-proteins, work in collaboration to facilitate global cytoskeletal organisation and a plethora of transport processes including cell migration, intracellular transport, tension sensing and cell division (O'Connell *et al*, 2007). While there are many classes of myosin, each contains an actin binding ATPase motor domain, which exerts force against actin, a lever arm or neck region that contains light chain binding IQ motifs, and a tail region which specifies cargo binding and other molecular interactions.

Although different classes of myosin perform very different cellular functions they all operate by the same basic mechanism, whereby the motor domain undergoes cyclical interactions with actin coupled to the breakdown of ATP. Each molecule of ATP that is converted to ADP and inorganic phosphate can generate movement along actin of between 5-25 nm and force of up to 5 pN. Regulation of acto-myosin motility is multi-faceted (Heissler & Sellers, 2016a), combining regulatory pathways operating via the actin track (historically called thin-filament regulation), or myosin-linked regulation (historically called thick filament regulation) which is often mediated via phosphorylation of the heavy chain or light chain(s) or by calcium-regulation of light chain binding (Heissler & Sellers, 2016b). It has been shown that phosphorylation at the conserved "TEDS" motif within the myosin motor domain of class 1 myosin affects acto-myosin interaction (Bement & Mooseker, 1995); phosphorylation within the tail region of class 5 myosin controls cargo binding (Rogers *et al*, 1999), whereas phosphorylation of class 2 myosin light chains and/or heavy chain can change the folded state of the heavy chain, affecting both actin interaction and ability to form filaments (Redowicz, 2001; Kendrick-Jones *et al*, 1987; Pasapera *et al*, 2015). So, phosphoregulation of myosin can occur in the head, neck and tail regions and also the light chains and its effects are manifold and vary across myosin classes and between paralogues within the same class. Its effect on

motile function is still not fully understood for many myosins, especially within yeast (East & Mulvihill, 2011).

The fission yeast, *Schizosaccharomyces pombe*, genome encodes for 5 myosin heavy chains from classes 1, 2, and 5 (Win *et al*, 2002), representing the basic subset of these actin-associated motor proteins found in eukaryotic cells. The single class 1 myosin, Myo1, is a 135 kDa protein, with motor domain, neck region (with two canonical IQ motifs) and a 49 kDa tail region containing a, so-called, tail-homology-2 domain, PH domain, SH3 domain and a carboxyl-terminal acidic region that associates with and activates the Arp2/3 complex to nucleate actin polymerisation (Lee *et al*, 2000). The myosin motor has a conserved TEDS site, phosphorylated by a Ste20 protein kinase, to modulate the protein's ability to associate with actin (Attanapola *et al*, 2009). Myo1 associates with membranes, primarily at sites of cell growth, where it is required for endocytosis, actin organisation and spore formation (Sirotkin *et al*, 2005; Lee *et al*, 2000; Itadani *et al*, 2007).

Calmodulin or calmodulin-like light chains associate with the IQ motifs within the myosin neck, providing a mechanism to regulate the length and stiffness of the lever arm (Trybus *et al*, 2007) and behaviour of the motor domain (Adamek *et al*, 2008). Calmodulins are ubiquitous calcium binding proteins that associate with and regulate the cellular function of diverse proteins. Calcium associates with up to four EF hand motifs within the calmodulin molecule to bring about a change in its conformation to modulate its affinity for IQ motifs within binding partner proteins (Crivici & Ikura, 1995). *S. pombe* encodes for two calmodulin like proteins, Cam1 and Cam2 (Takeda & Yamamoto, 1987; Itadani *et al*, 2007). Cam1 is a typical calmodulin that associates with IQ domain containing proteins in a calcium dependent manner, to affect functions as diverse as endocytosis, spore formation, cell division or maintaining spindle pole body integrity (Takeda & Yamamoto, 1987; Moser *et al*, 1995; 1997; Itadani *et al*, 2010). Unlike Cam1, Cam2 is not essential and is predicted to be insensitive to calcium, however like Cam1 it has been reported to regulate Myo1 (Sammons *et al*, 2011; Itadani *et al*, 2007). While cells lacking Cam2 show defects in spore formation they have no significant growth-associated phenotypes during the vegetative growth cycle.

TOR (Target of Rapamycin) signaling plays a key role in modulating cell growth in response to changes in cell cycle status and environmental conditions (Laplante & Sabatini, 2012). The mTOR kinase forms two distinct protein complexes TOR complex 1 (TORC1) and TORC2, each defined by unique components that are highly conserved across species. While both TORC1 and TORC2 have been implicated in the control of cell migration and F-actin organisation (Liu & Parent, 2011), TORC2 plays a key role in regulating the actin cytoskeleton in yeasts, *Dictyostelium discoideum* and mammalian cells (Jacinto *et al*, 2004; Baker *et al*, 2016; Lee *et al*, 2005). While the basic principle of control of each regulatory signal (e.g. phosphorylation and calcium signalling) are understood, the interplay between parallel modes of regulation is relatively unknown. *S. pombe,* contains both TORC1 and TORC2 complexes (Petersen, 2009).

In the current study, we have used molecular cell biological, biochemical and single molecule techniques to help identify and characterise a novel TORC2 phosphorylation-dependent system for regulating calcium-dependent switching of different calmodulin light chain(s) binding to the neck region of Myo1. We have established the contribution that each calmodulin plays in regulating this conserved motor protein and how they affect the conformation of the myosin lever arm. We propose a concerted mechanism of regulation by both calcium and phosphorylation that controls motility and function of Myo1 in response to signals controlling cell cycle progression.

Results

Fission yeast myosin-1 is phosphorylated within the IQ neck domain.

Analysis of extracts from exponentially growing fission yeast cells indicates its sole class I myosin, Myo1, is subject to multiple phosphorylation events (Figure 1A). Phosphoproteomics studies (Carpy *et al*, 2014; Wilson-Grady *et al*, 2008) revealed a conserved phosphoserine residue located within the IQ motif containing neck region of class I & V myosins (Figure 1B). The location of this AGC family kinase consensus phosphoserine site (Pearce *et al*, 2010) has the potential to impact myosin activity and function by affecting conformation of the lever arm as well as light chain binding. A phosphospecific antibody was raised to confirm phosphorylation of the Myo1 serine 742 (Myo1^{S742}), and established that it is phosphorylated in a TORC2 signalling and growth media dependent manner (Figure 1C-E). Consistent with the TORC2 dependent pathway modulating cell growth in response to media quality (Petersen & Nurse, 2007), replacing the serine with a non-phosphorylatable alanine residue within *myo1.S742A* cells resulted in an inability to inhibit growth when cultured in media containing minimal nitrogen (Figure 1F).

Phosphorylation modulates Myo1 lever arm length.

As serine 742 lies within the IQ motif containing neck region of myosin-1, we explored whether Myo1^{S742} phosphorylation affects calmodulin binding and conformation of the neck region. Isoforms of the Ca^{2+} sensitive fission yeast calmodulin (Cam1 and Cam1.T6C) were isolated in their native amino-terminally (Nt) acetylated forms using bacteria co-expressing the fission yeast NatA amino-α-acetyl-transferase complex (Eastwood *et al*, 2017). A FRET based fusion was generated with CyPet donor and YPet acceptor fluorophores (Nguyen & Daugherty, 2005) juxtaposed around the Cam1 protein to monitor Ca^{2+} dependent changes in Cam1 conformation (Figure 2A). This FRET-Cam1 fusion (Figure 2B), and Nt-acetylated IAANS labelled Cam1.T6C (Figure 2C) established Ca^{2+} binding brings about a change in the Cam1 conformation. Calculated pCa values for the Cam1-FRET (Figure 2B pCa_{50}: 6.12), reflect global change in Cam1 conformation, while the IAANS dependent pCa (Figure

2C pCa_{50}: 6.54) reflects Ca^{2+} dependent changes in the local environment at the amino lobe of Cam1. Quin-2, fluorescence of which increases upon Ca^{2+} binding (Tsien, 1980), was used to establish Ca^{2+} ions release from Cam1 with 3 distinct rate constants (137, 12.9 and 2.0 s^{-1}) (Figure 2D).

To characterise Cam1 binding to the IQ neck region of the fission yeast myosin-1, recombinant FRET constructs were produced in which CyPet and YPet were separated by individual or both Myo1 IQ motifs ($Myo1^{IQ1}$-FRET, $Myo1^{IQ2}$-FRET, $Myo1^{IQ12}$-FRET) (Figure 2E & S1). Cam1 binding to the IQ motif(s) stabilises the α-helix and results in a calcium regulated drop in FRET signal (Figure 2E-F). Analysis of interactions between Cam1 and $Myo1^{IQ12}$-FRET revealed Cam1 molecules associated with the combined $Myo1^{IQ12}$ motifs with 2 distinct phases, each contributing 50% of the overall change in signal (Figure 2G). The first Cam1-$Myo1^{IQ12}$ binding event corresponds to an affinity of less than 0.1 μM (binding was too tight to calculate affinity with higher precision), while the second event correlates with an approximately 10-fold weaker binding affinity (0.68 μM). This association was seen to be sensitive to calcium (pCa of 5.87) (Figure 2I), illustrating Cam1 only associates with Myo1 in low cellular Ca^{2+} concentrations. Interestingly while Cam1 was seen to bind tightly to $Myo1^{IQ1}$ alone (K_d<0.1 μM), no detectable association was observed for the equivalent single $Myo1^{IQ2}$ motif (Figure 2J). Together these data are consistent with a sequential cooperative binding mechanism by which the stable residency of Cam1 in the first IQ position is required before calmodulin can bind to $Myo1^{IQ2}$.

Replacing serine 742 within the IQ neck region with a phosphomimetic aspartate residue had no significant impact upon the affinity, calcium sensitivity or cooperative nature of the interaction between Myo1 and Cam1 (Figure 2G). However, the phosphomimetic replacement resulted in a change in maximum FRET signal upon Cam1 binding (F_{max} 46.05 vs 31.64) (Figure 2G & H) indicating $Myo1^{S742}$ phosphorylation changes the conformation of the lever arm upon Cam1 binding, rather than modulating the affinity for Cam1.

Phosphorylation regulates Myo1 dynamics and endocytosis.

To explore *in vivo* Myo1 and calmodulin dynamics we generated prototroph *S.*

pombe strains in which endogenous *myo1, cam1, or cam2* genes were fused to cDNA encoding for monomeric fluorescent proteins (Figure 3A). Using high-speed (20 Hz) single molecule TIRF analysis we explored how Myo1^{S742} phosphorylation impacts Myo1 and Cam1 dynamics and function within the cell. Myo1 and Cam1 associated with the cell membrane in two distinct ways: we observed rapid transient associations of single molecules at the cell membrane, characterised by low-intensity single stepwise changes in intensity as well longer endocytic events which were much brighter and had a very different time-course. Single molecules of Myo1 and Cam1 bound transiently at the cell membrane and moved with low mobility (0.03 $\mu m^2.s^{-1}$), ~10-times slower than diffusion of integral membrane proteins (Mashanov *et al*, 2010). The individual, diffraction-limited fluorescent spots appeared and disappeared in a stepwise fashion (i.e. within a single video frame). Event durations were exponentially distributed with mean lifetime of 2.2 s^{-1} (n = 152) (Movie 1). In contrast, during endocytic events, the fluorescence signal increased gradually, rising to a peak amplitude consistent with ~45 molecules of mNeongreen.Myo1 (rate ~13 molecules.s^{-1}), which dwelled for ~6 s, before falling to baseline (rate ~14 molecules.s^{-1}) (Figure 3B, Movie 2). The estimated number of Myo1 molecules is lower than reported in an earlier study (Sirotkin *et al*, 2010) perhaps due to differences in imaging techniques, as TIRF imaging illuminates the specimen to a depth of ~100nm whereas confocal imaging would extend to > 400nm). The duration (T_{dur}) of endocytic events (measured as described in the Methods) was 13.84 s +/- 0.39 (mean +/- SEM, n=50) (Figure 3C) and while there was significant variation in the maximum mNeongreen.Myo1 intensity (2373 +/- 155), there was no correlation between maximum intensity and event duration (Figure 3D). Fluorescence intensity dynamics of Cam1.GFP during endocytic events were similar to mNeongreen.Myo1, but T_{dur} was significantly shorter (P <0.0001), 10.99 s +/- 0.21 (n=52) while the peak intensity was roughly double that measured for mNeongreen.Myo1 and equivalent to ~ 90 GFP molecules (Figure 3E) consistent with Cam1 occupying both IQ sites within the Myo1 neck region. The briefer event duration observed for Cam1 might be explained by Cam1 dissociating from Myo1 before Myo1 leaves the endocytic patch. This idea was confirmed using two-colour imaging of *mNeongreen.myo1 cam1.mCherry* cells which showed Myo1 and Cam1 arrived simultaneously at

the endocytic patch, but Cam1.mCherry disassociated ~3 s before mNeongreen.Myo1 (Figure 3F, S2).

Analysis of Myo1 and Cam1 dynamics in *myo1.S742A* cells during endocytosis revealed Myo1^{S742A} had average assembly/disassembly rates and plateau intensity identical to wild type Myo1, but T_{dur} was 1.5 sec shorter (12.3s +/- 0.31 n=67) (Figure 3G & S2). Consistent with the *in vitro* data, the *myo1.S742A* mutation did not impact on the ability of Cam1 molecules associating at both IQ motifs, as average assembly/disassembly rates, and plateau intensity for Cam1 were the same in both wild type and *myo1.S742A* cells. However, we found that Myo1^{S742A} and Cam1 proteins disassociated simultaneously and somewhat earlier during the endocytic event in this strain.

These TIRF imaging data were consistent with widefield 3D-timelapse imaging that showed lifetimes of Myo1 and Cam1 foci were shorter in *myo1.S742A* cells when compared to *myo1*$^{+}$ (Figure 3H). In contrast, while the *myo1.S742A* allele did not affect accumulation of Cam2 or LifeACT to sites of endocytosis (Figure 3I), the rate of endocytosis differs between old end and new ends of *myo1-S742A* cells compared to wild type (Figure 4A). Therefore, while Myo1^{S742} phosphorylation does not impact assembly of Myo1-Cam1 endocytic foci, it regulates myosin activity to change the function of the ensemble of endocytic proteins during bipolar growth.

Myo1 S742 is phosphorylated in a cell cycle dependent manner to regulate polarised cell growth.

Upon cell division fission yeast cells grow exclusively from the old cell end that existed in the parental cell. At a point during interphase (called New End Take Off -NETO) there is a transition to a bipolar growth (Mitchison & Nurse, 1985). This cell cycle switch in growth pattern correlates precisely with a parallel redistribution of endocytic actin patches (Marks & Hyams, 1985). As the *myo1.S742A* allele only affected actin dynamics at the old cell end during bipolar growth we examined whether this post-translational modification was subject to cell cycle dependent variance. Analysis of extracts from cell division cycle mutants arrested in G1 (*cdc10.v50* cells) or late G2 (*cdc25.22* cells)

revealed Myo1^{S742} is phosphorylated in a cell cycle dependent manner (Figure 4B). This was confirmed by monitoring Myo1^{S742} phosphorylation in cells synchronised with respect to cell cycle progression (Figure S3). These data established that Myo1^{S742} phosphorylation peaks in early interphase (G1 cells), prior to the transition to a bipolar growth pattern, and steadily decreases until becoming undetectable towards the end of G2. Analysis of growth kinetics revealed *myo1.S742A* cells grow slower than wild type (Figure 4C), and have a longer average length (*myo1*$^{+}$: 9.77 ± 1.77 µm; *myo1.S742A*: 13.2 ± 2.47 µm. t-test >99% significance n>500). In addition, a significant proportion of *myo1.S742A* cells demonstrate polarity defects, with 24.7% of cells having a bent morphology (i.e. growth deviates by >5º from longitudinal axis), compared to 1% seen in wild type (Figure 4D-E). Consistent with these observations, *myo1.S742* mutants exhibit defects in the transition from monopolar to polar growth. Cell wall staining revealed a significantly higher proportion of *myo1.S742A* cells exhibit monopolar growth compared to equivalent wild type, indicating disruption in the switch from monopolar to bipolar growth (Figure 4E). This was confirmed by tracking the cellular distribution of the actin patch marker, Sla2/End4, following cell division. Sla2 failed to redistribute to the newly divided end of *myo1.S742A* cells during interphase (Figure 4F). Together these data show that cell cycle variation in Myo1^{S742} phosphorylation modulates the myosin lever arm to regulate endocytosis and polarised growth.

Cam2 associates with internalised endosomes and not Myo1 during vegetative growth.

Myo1 has been reported to associate with a second calmodulin like protein, Cam2, via its second IQ motif (Sammons *et al*, 2011). However, our data indicate Cam1 occupies both Myo1 IQ motifs during endocytosis. Widefield microscopy revealed Myo1 and Cam1 dynamics (Figure 5A) at endocytic foci differ significantly from Cam2 which is recruited to sites of endocytosis later than Myo1 and Cam1, but prior to budding off, where, like CAPZA^{Acp1}, Sla2 and actin, it remains associated with laterally oscillating internalised endosomes (Figure 5B-C). Similarly, simultaneous imaging of Cam1 and Cam2 in *cam1.mCherry cam2.gfp* cells revealed each protein localises to many foci

297 lacking the other calmodulin, indicating differences in the timing of endocytic
298 recruitment (Figure 5D). While Cam1 recruitment to endocytic foci is abolished
299 in the absence of Myo1 (Figure 5E), the intensity, volume and number of Cam2
300 foci increases in the absence of Myo1 (Figure 5F Table 1). However,
301 internalisation and lateral "oscillating" dynamics of Cam2, and actin were
302 dependent on Myo1 (Figure 5F & G). Therefore, while Cam1 and Cam2 both
303 localise to sites of endocytosis, they appear to do so at different times, and each
304 have differing Myo1 dependencies.

305 TIRF analysis revealed on average a total of ~30 Cam2 molecules recruit to
306 each endocytic foci, and the kinetics of its recruitment to foci differ significantly
307 to that observed for both Myo1 and Cam1. Cam2 often had a linear binding
308 relationship (Figure 6A), which contrasts to the sigmoidal profiles observed for
309 Myo1 and Cam1 (Figure 3C & E). TIRFM confirmed Cam2 remained associated
310 with endocytic vesicles after they were internalised and their connection with
311 the cell membrane was broken (Movie 3). Background corrected intensity
312 traces of Cam2 dynamics at the membrane patch before, during, and after the
313 end of endocytosis showed the signal rapidly dropped to baseline (<1s) (Figure
314 6A), with the Cam2 labelled vesicles remaining visible close to the membrane
315 at the limit of the evanescent field. A large number of these mobile internalised
316 Cam2 labelled vesicles were seen moving within the cytoplasm with relatively
317 low cytosolic background signal (Movie 3), indicating much Cam2 associates
318 with endocytic vesicles and remains bound to mature endosomes. During the
319 latter stages of endocytosis, Cam2 was internalised on the endosome while
320 Myo1 remained at the plasma membrane during endosome abscission (Sirotkin
321 *et al*, 2010; Berro & Pollard, 2014; Picco *et al*, 2015). Timing of the Myo1 and
322 Cam2 fluorescence signals did not correlate; Cam2 was associated with the
323 endocytic vesicle moving away from the cell surface during endocytosis and
324 remaining associated with the early endosome at the time of scission. Whereas,
325 Myo1 and Cam1 remained immobile and stayed close to the cell surface
326 (plasma membrane) throughout the endocytic cycle.

327 To correlate Myo1-Cam1 association at sites of endocytosis with scission of the
328 endosome into the cytoplasm, we followed Cam1 and Cam2 dynamics
329 simultaneously in *cam1.mCherry cam2.gfp* cells (Movie 4). An average curve

generated from profiles of >30 complete individual endocytic events (Figure 6B) shows Cam2 moves away from the cell surface shortly after Cam1 leaves but before Myo1, with the time of abscission (T_{scis}) occurring on average 13.4 sec after the event starts (T_{start}). Therefore endosome scission takes place during the Myo1 disassembly phase, and around the time Cam1 dissociates from Myo1.

Intriguingly, while the overall distribution of Myo1 and Cam1 appeared unaffected in *cam2*Δ cells, the number, volume and intensity of foci were significantly reduced (Figure 6C-D Table 1). TIRF-based analysis of the spatial distribution of Myo1 and Cam1 at endocytic foci revealed that Cam1 organised into more dispersed foci in the absence of Cam2 (Figure 6E-F), indicating Cam2 plays a role in organising the Myo1-Cam1 complex at the plasma membrane.

Serine 742 phosphorylation increases the affinity of a single Cam2 for Myo1.

In vitro analysis revealed two Cam2 molecules can associate with the unphosphorylated $Myo1^{IQ12}$ region (Figure 6G) with 2 distinct phases. In contrast to Cam1 binding, 70% of the signal change is associated with an affinity of 1.10 μM. The smaller tighter signal change is not accurately measurable, but the combined change in signal is consistent with 2 binding events. As predicted from sequence analysis, Cam2 was not seen to associate with calcium (Figure 2D), and its conformation and interactions with Myo1 were insensitive to the divalent cation (Figure 6H). Like Cam1, Cam2 had a higher affinity for the first IQ motif (0.4 μM) than both IQ12 together, and did not bind to IQ2 alone (Figure 2J). Cam1 calcium binding, as measured by IAANS labelling or change in Quin-2 fluorescence were unaffected by Cam2, while gel filtration and fluorescence binding assays provided no evidence of a direct physical interaction between the two proteins (Figure S4). Interestingly a difference was observed in fluorescence amplitudes between Cam1 and Cam2 binding to the IQ12 motif, may indicate an impact upon lever arm length, (Figure 6H), potentially providing a mechanism to directly control Myo1 motor activity. $Myo1^{S742}$ phosphorylation had no measurable impact upon the dynamics and

362 distribution of Cam2 within fission yeast cells undergoing normal vegetative
363 growth (Figure 7A Table 1). In contrast, *in vitro* analysis revealed Cam2 was
364 only able to occupy one of the two IQ motifs in the Myo1$^{S742D\text{-}IQ12}$ protein, be
365 that with an increased affinity to the unphosphorylated protein (0.25 μM) (Figure
366 6G), indicating Cam2 impacts Myo1 function outside of the vegetative life cycle.

367

368 **Cam1 and Cam2 associate with Myo1 during meiosis.**

369 Calcium levels within log phase yeast cells are relatively low (100-200 nM) (Ma
370 *et al*, 2011; Miseta *et al*, 1999), and provides favourable conditions for Cam1 to
371 associate with Myo1 (pCa - 5.87). Analysis of cell fluorescence indicated the
372 relative abundance of Myo1 : Cam1 : Cam2 within the *S. pombe* cell to be 0.2
373 : 1.45 : 1 (Table 1), which is similar to the ratios defined by quantitative
374 proteomic analysis of 0.45 : 1.56 : 1 (Marguerat *et al*, 2012). Similarly, image
375 analysis of Cam1-GFP fluorescence revealed 1.7% of Cam1 to be associated
376 with discrete foci within cells (Table 1), 40% of which is dependent upon Myo1,
377 with the majority associating with the SPB (Figure 5D). This indicates ~0.68%
378 of cellular Cam1 associates with Myo1 at dynamic endocytic foci. These relative
379 protein levels, binding affinities and low Ca^{2+} concentrations favour Cam1
380 binding to Myo1, over Cam2 at both IQ sites (Figure 7B), consistent with *in vivo*
381 observations.

382 While Ca^{2+} levels are low during vegetative growth, sporadic prolonged calcium
383 bursts occur upon pheromone release during mating (Carbó *et al*, 2016; Iida *et*
384 *al*, 1990), and levels elevate significantly (~10 fold) during the subsequent
385 meiosis and sporulation (Suizu *et al*, 1995). Cam1 would be less likely to bind
386 to Myo1 in these conditions (pCa 5.87). Myo1^{S742} is phosphorylated from G1,
387 through cell fusion, persisting until completion of spore formation (Figure 7C).
388 In addition Cam2 abundance increases significantly in relation to Cam1 during
389 G1 upon mating and entry into meiosis (Mata & Bähler, 2006; Mata *et al*, 2002).
390 These provide conditions that would favour Myo1-Cam2 interactions over
391 Cam1 (Figure 7B), which is consistent with both Myo1 and Cam2 playing
392 important role at the leading edge of forespore membrane formation during
393 meiosis (Toya *et al*, 2001; Itadani *et al*, 2007). Consistent with this prediction,

Myo1, Cam1, Cam2 foci lifetime and dynamics differ significantly to those observed in vegetative cells ($P<0.0001$), lasting significantly longer (>1 min) in meiotic and sporulating cells (Figure 7D & E). In contrast to vegetative cells, during meiosis and subsequent spore formation, like Myo1 and Cam1, Cam2 and actin foci were less dynamic, lacking any oscillation and remain in a fixed position with significantly longer lifetime than within actively growing cells (Figure 7D, Movie 5-8).

Finally, we used the *myo1.S742A* allele to explore the impact of Myo1^{S742} phosphorylation on Myo1, Cam1 and Cam2 dynamics and function during meiosis. In contrast to wild type, the lifetime of Cam1 foci were significantly shorter in *myo1.S742A* cells, and did not correlate with Myo1 and Cam2 dynamics, both of which differed significantly from *myo1*$^{+}$ cells (Figure 7F). The majority of Cam2 foci remained present in the cell for greater than 2 mins in meiotic cells lacking Myo1^{S742} phosphorylation, which also differed significantly from Myo1^{S742A} dynamics, indicating normal Cam1 and Cam2 interactions with Myo1 were abolished. Consistent with *myo1.S742A* cells grown to stationary phase in minimal media (Figure 1F), heterothallic (h^{90}) G1 arrested nitrogen starved *myo1.S742A* cells failed to inhibit polar growth (Figure 7G), mating cells accumulated with abnormal shmoo tips, and meiosis often resulted in cells with too few unequally sized spores (Figure 7G arrowheads). This spore defect phenotype is similar to that observed in *cam2*Δ cells (Itadani *et al*, 2007), which is consistent with a model whereby increase in cellular Ca^{2+} and Myo1^{S742} phosphorylation are both key for Cam2 association with and regulation of Myo1.

These data support a model by which changes in calcium levels and TORC2 dependent phosphorylation status provide a simple two stage mechanism for modulating motor activity by modifying lever arm length as well as switching calmodulin light chain preference to regulate myosin function in response to changing needs of the cell (Figure 7B).

Discussion

Myosins are subject to diverse systems of regulation, which include composition of the actin track, cargo and light chain interactions, as well as phosphorylation. Here we describe a newly discovered mechanism by which phosphorylation of the myosin heavy chain (Figure 1) regulates light chain specificity, lever arm conformation and flexibility, to modulate and control cellular function. During the vegetative life cycle, within basal levels of cellular calcium, the fission yeast myosin-1 preferentially associates with two molecules of the calcium regulated calmodulin light chain Cam1 (Figures 2 & 3). During early stages of the cell cycle TORC2 dependent phosphorylation of the Myo1 neck region, to which the light chain(s) bind, changes the length of the Cam1 associated lever arm to moderate its activity to regulate the rate of endocytosis (Figure 4).

During the sexual cycle, Myo1^{S742} remains phosphorylated (Figure 7). This combined with the increase in cytosolic Ca^{2+} levels leads to a switch in light chain preference to a single molecule of the calcium insensitive calmodulin like, Cam2. The single Cam2 molecule is likely to bind IQ1 of S742 phosphorylated Myo1, as comparison with the structure of the IQ region of Myosin-1 and calmodulin (Lu *et al*, 2014), phosphorylation of S742 is likely to impact calmodulin interactions at the 1st IQ position. Furthermore, our data reveals that Cam2 is unable to associate with IQ2 alone, as it is necessary for one calmodulin to occupy IQ1 in order for a second to bind to IQ2. This switch in light chain occupancy may provide a mechanism to change the stiffness of the Myo1 neck region (i.e. the “lever arm”) and thereby modulate the movement and force it produces during the acto-myosin ATPase cycle and/or the load-sensitivity of its actin-bound lifetime.

While Myo1 is capable of associating with phospholipid membranes via its Plekstrin Homology (PH) domain, *in vivo* data suggests that this alone is not sufficient to enable a stable interaction at the plasma membrane (Figure 8A). The build-up of the early endocytic markers, such as Pan1 or Sla1, are necessary to catalyse its nucleation to early endocytic patches allowing Myo1 foci to form at the site of membrane invagination. This is consistent with our observation that once initiated, Myo1-Cam1 foci do not collapse, but go on to

455 complete the endocytic event (Figure 8B) (Sun *et al*, 2015; Barker *et al*, 2007).
456 Similarly, the size of this early marker "patch" has a direct impact upon the
457 number of Myo1 molecules recruited to the plasma membrane, which is
458 consistent with the role of Pan1 in enhancing the Arp2/3 actin nucleating activity
459 of myosin-1 foci in yeast (Barker *et al*, 2007).

460 The local concentration of Myo1 at the endocytic patch appears critical, rather
461 than the absolute number of Myo1 molecules, as the latter does not affect the
462 duration of the Myo1 driven event. Indeed the duration of Myo1's residency at
463 the plasma membrane is driven by Cam1 and phosphorylation regulated neck
464 length. Interestingly neither of these factors affect the rate of Myo1 or Cam1
465 recruitment or disassociation from the membrane.

466 Therefore the size of the Pan1 patch determines the number of Myo1 molecules
467 necessary to generate a critical local concentration of Arp2/3 nucleated actin
468 filaments (Figure 8C) (Barker *et al*, 2007). At the critical concentration myosin
469 heads are able to interact with actin filaments nucleated from either adjacent
470 Myo1 tails or WASP activated Arp2/3 complexes, tethered to the membrane via
471 molecules such as the Talin like Sla2 (Figure 8D) (Sirotkin *et al*, 2005; 2010).
472 The Myo1 is then primed to act as a tension sensor against the actin filament,
473 as it pushes against the membrane of the internalised endosome, which grows
474 against the significant 0.85 MPa (8.3 atm) turgor pressure within the cell (Minc
475 *et al*, 2009) (Figure 8E). While observations within budding yeast indicate motor
476 activity from a ring of myosins at the lip of the endosome (Mund *et al*, 2018) is
477 necessary for endocytic internalisation the mechanism by which the myosin
478 interacts with actin to facilitate this is unknown (Sun *et al*, 2006).

479 The number of Myo1 molecules at the plasma membrane foci remains constant,
480 as the membrane is internalised, until 2 seconds after Cam1 disassociates from
481 Myo1 (Figure 8F). While the trigger for Cam1 release is unknown, the rapid
482 ensemble nature of the event indicates it is likely to be initiated by a rapid
483 localised spike in calcium. This could perhaps be driven by a critical level of
484 membrane deformation coupled to calcium influx - similar to processes
485 proposed for mechano-transduction and the role of mammalian myosin-1 within
486 the stereocilia of the inner ear (Adamek *et al*, 2008; Batters *et al*, 2004).
487 Alternatively, mechanical forces acting on Myo1 may drive Cam1 dissociation.

Genetics studies from budding yeast indicate that calmodulin mutants, unable to bind Ca^{2+}, release normally from myosin-1 (Geiser *et al*, 1991). Research using mammalian brush border myosin-1, indicates that changes in lipid composition of membranes to which the motor is associated are sufficient to displace calmodulin from the IQ region (Hayden *et al*, 1990). In fission yeast this change in lipid could be rapidly triggered by PI4-kinase phosphorylation (Cam2 is the light chain for PI4 kinase (Sammons *et al*, 2011)). This is consistent with timing of Cam2 membrane recruitment and could go some way to explain why Myo1 foci are more dispersed in absence of Cam2.

Once Cam1 detaches from the Myo1 molecule, the neck loses rigidity (Figure 8F), reducing tension between the myosin motor and actin filament, causing it to detach rapidly from F-actin (Lewis *et al*, 2012; Mentes *et al*, 2018). Given the off-rate of single Myo1 molecules from the plasma membrane is ~2 sec^{-1} (Figure 3B), lack of association with actin would mean that Myo1 would leave the endocytic patch a second or so after losing its Cam1 light chain. Together these events account for the 2 sec delay between disappearance of Cam1 and Myo1 from the membrane. The same drop in tension at the plasma membrane could provide the signal for scission of the endosome (Palmer *et al*, 2015).

The conformation and rigidity of the Myo1 lever arm would therefore play a key role in modulating the tension sensing properties of the motor domain. This is consistent with our data, where wild type phosphorylatable Myo1 resides at the membrane ~1.8 sec longer than unphosphorylated $Myo1^{S742A}$ (Figure S2). Phosphorylation-dependent changes in the conformation of the myosin neck provide a simple mechanism to modulate the rate of endocytosis according to the size and needs of the cell. Similarly, in the presence of Ca^{2+} and $Myo1^{S742}$ phosphorylation, a single Cam2 resides at IQ1 motif of the neck (Figure 7B), again modulating neck conformation adjacent the motor domain as well as allowing flexibility within the carboxyl half of the neck region. This would provide a relatively tension insensitive motor, that stalls against the actin polymer, and would therefore persist significantly longer at the endocytic foci, as observed here (Figure 7E). These changes in lever arm properties change the overall rate of endocytosis, as observed in differences for actin labelled endosomes to internalise (Figure 4A).

Thus phosphorylation-dependent changes in the calcium regulated conformation and rigidity of the myosin lever arm could provide a universal mechanism for regulating the diverse cytoplasmic activities and functions of myosin motors within all cells.

Materials and Methods

Yeast cell culture: Cell culture and maintenance were carried out according to (Moreno *et al*, 1991) using Edinburgh minimal medium with Glutamic acid nitrogen source (EMMG) unless specified otherwise. Cells were cultured at 25 ºC unless stated otherwise and cells were maintained as early to mid-log phase cultures for 48 hours before being used for analyses. Genetic crosses were undertaken on MSA plates (Egel *et al*, 1994). All strains used in this study were prototroph and listed in Supplementary Table 1.

Molecular Biology: *cam1*$^{+}$ (SPAC3A12.14), *cam1.T6C* and *cam2*$^{+}$ (SPAC29A4.05) genes were amplified as *Nde1* - *BamH1* fragments from genomic *S. pombe* DNA using o226/o227 and o393/o394 primers and cloned into pGEM-T-Easy (*Promega*, Madison, WI, USA). After sequencing the subsequent genes were cloned into pJC20 (Clos et al., 1990) to generate bacterial calmodulin expression constructs. DNA encoding for the FRET optimized fluorophores CyPet and YPet (Nguyen and Daugherty, 2005) were each amplified using primers o405 / o406 and o403 / o404 respectively. o406 also incorporated DNA at the 3' end of the CyPet ORF encoding for the first IQ motif of the Myo1 neck region, while o404 included DNA encoding a Gly3His6 tag at the 3' of the YPet ORF. The two DNA fragments were cloned into pGEM-T-Easy in a three-way ligation reaction to generate pGEM-CyPet-Myo1IQ1-YPet. The CyPet-Myo1^{IQ1}-YPet DNA was subsequently sequencing and cloned as a Nde1 - BamH1 fragment into pJC20 (Clos & Brandau, 1994) to generate pJC20CyPet-Myo1^{IQ1}-YPet. Complementary oligonucleotides o425 & o426 were annealed together and ligated into BglII – Xho1 cut pJC20CyPet-Myo1^{IQ1}-YPet to generate pJC20CyPet-Myo1^{IQ12}-YPet. Similarly, complementary oligonucleotides o429 & o430 were annealed together and subsequently ligated into Sal1-BglII cut pJC20CyPet-Myo1^{IQ1}-YPet and the subsequent Xho1 fragment was excised to generate pJC20CyPet-Myo1^{IQ2}-YPet. Site directed mutagenesis was carried out using pJC20CyPet-Myo1^{IQ12}-YPet template and o427 & o428 primers to generate pJC20CyPet-Myo1^{IQ12}S742D-YPet. Complementary oligonucleotides o449 & o450 were annealed together and ligated into Nru1 – Xho1 digested pJC20CyPet-Myo1^{IQ12}S742D-YPet to generate pJC20CyPet-Myo1^{IQ12}S742A-YPet. All plasmids were sequenced

upon construction. Strains with fluorophore tagged alleles of *cam1*$^+$ and *cam2*$^+$ were generated as described previously using appropriate template and primers (Bähler *et al*, 1998). Strains in which the *myo1.S742A*, *myo1.S742D*, *mNeongreen-myo1*, *mNeongreen-myo1.S742A*, or *mNeongreen-myo1.S742D* alleles replaced the endogenous *myo1*$^+$ gene (SPBC146.13c) were generated using a marker switching method (MacIver *et al*, 2003). Oligonucleotides are described in Supplementary Table 2.

Protein expression & purification: All recombinant proteins were expressed and purified from BL21 DE3 *E. coli* cells, except Cam1 proteins where BL21 DE3 pNatA cells (Eastwood *et al*, 2017) were used to allow amino-terminal acetylation (Figure S1). *Calmodulin purification*: Cell lysates were resuspended in Buffer A (50 mM Tris, 2 mM EDTA, 1 mM DTT, 0.1 mM PMSF, pH 7.5) and precleared by high speed centrifugation (48,500 RCF; 30 min; 4 °C), before ammonium sulphate was added to the supernatant at 35 % saturation, incubated for 30 minutes at 4 °C. Precipitated proteins were removed by centrifugation (48,500 RCF; 30 min; 4 °C). For Cam1 purifications the precipitation cleared supernatant was added to a pre-equilibrated 10 ml phenyl sepharose (CL-4B) column (Buffer B: 50 mM Tris, 1 mM DTT, 1 mM NaN_3, 5 mM $CaCl_2$, pH 8.0), washed in 4 volumes of Buffer B before eluted as fractions in Buffer C (50 mM Tris, 1 mM DTT, 1 mM NaN_3, 5 mM EGTA, pH 8.0). For Cam2 purification the precipitation cleared supernatant underwent a second round of ammonium sulphate precipitation and clearing, and the subsequent supernatant subjected to isoelectric precipitation (pH 4.3) and centrifugation (48,500 RCF: 30 minutes; 4 °C). The resultant pellet was resuspended in Buffer A, heated to 80 °C for 5 minutes and denatured proteins removed by centrifugation (16,000 RCF; 5 min). *His-tagged* proteins were purified in native conditions using prepacked, pre-equilibrated 5ml Ni^{2+} columns.

Fast reaction kinetics: All transient kinetics were carried out using a HiTech Scientific DF-61 DX2 Stopped Flow apparatus (TgK Scientific, Bradford-upon-Avon, UK) at 20ºC. All data was acquired as the average of 3-5 consecutive shots and analysed using the KineticStudio software supplied with the equipment. Quin-2 fluorescence was excited at 333 nm and used a Schott GG445 cut off filter to monitor fluorescence above 445 nm. IAANS (2-(4'-

(iodoacetamido)anilino)-naphthalene-6-sulfonic acid) was excited at 335 nm and fluorescence was monitored through a GG455 filter. For the FRET measurements, CyPet was excited at 435 nm and YPet emission was monitored through a combination of a Wrattan Gelatin No12 (Kodak) with a Schott GG495 nm filter to monitor fluorescence at 525-530 nm.

Fluorescence spectra: Emission spectra were obtained using a Varian Cary Eclipse Fluorescence Spectrophotometer (Agilent Technologies, Santa Clara, CA) using a 100 µl Quartz cuvette. For FRET measurements samples were excited at 435 nm (CyPet excitation) and emission was monitored from 450 – 600 nm with both slits set to 1 nm. Affinity experiments were carried out using 1 µM IQ-FRET protein with varying concentrations of Cam1 or Cam2 in a final volume of 100 µl in analysis buffer of 140 mM KCl, 20 mM MOPS, pH 7.0 with or without 2 mM $MgCl_2$ and with 2 mM of EGTA, $CaCl_2$ or Ca^{2+}-EGTA as required.

Live cell imaging: Live cell widefield fluorescence imaging was undertaken as described previously (Baker *et al*, 2016). For Total Internal Reflection Fluorescence Microscopy (TIRFM) *S. pombe* cells were immobilized on №1, Ø 25 mm lectin coated coverslips and placed into imaging chambers filled with EMMG medium. A previously described custom TIRF Microscope (Mashanov *et al*, 2003) was used to image individual cells at a rate of 20 fps in either single of dual colour mode. Lasers: 488 nm/100 mW and 561 nm/150 mW (*Omicron*, Germany); emission filters 525/50 nm and 585/29 nm, dichroic mirror 552 nm (*Semrock*, NY); all lenses and mirrors (*Thorlabs*, NJ), except two Ø 3 mm mirrors (*Comar Optics*, UK) which directed light in and out of the 100× 1.45 NA objective lens (*Olympus*, Japan). Sequences of images were captured using one or two iXon897BV cameras (*Andor Technology*, UK) with custom made acquisition software. 100% laser power (488 nm) was used to image individual mNeongreen-Myo1 and Cam1-GFP molecules. The laser intensity was reduced to ≤ 20% during endocytosis imaging experiments to minimize photobleaching. All imaging was undertaken at 23 °C.

Image analysis: *Widefield data* was analysed using Autoquant software (*MediaCybernetics*, Rockville, MD, USA). All 3d image stacks were subjected to blind 3d deconvolution before analysis. Average size and number and

cellular distribution of foci were calculated from all foci present within ≥ 30 cells for each sample examined. Timing of foci events were calculated from kymographs generated in Metamorph software (*Molecular Devices*, Sunnyvale, CA, USA). The proportion of cells displaying a bent cell phenotype was determined from more than >350 calcofluor (1 $mg.ml^{-1}$) stained cells for each strain. Bent cells were defined by a deviation in the direction of growth of > 5º from the longitudinal axis. *TIRF data* analyses, including single molecule detection and tracking, was undertaken using GMimPro software (Mashanov & Molloy, 2007). Endocytic events were identified by creating an image representing the standard deviation of each pixel over the whole video sequence (known as a "z-projection"). Bright spots in this image correspond to regions of the yeast cell that showed large intensity fluctuations. Regions of interest (ROIs) ~ 0.5 µm diameter (5x5 pixels) were created to enclose the site of endocytosis and changes in the averaged ROI intensity over the entire video record were saved for future analysis. To correct for local variation in background signal, the average intensity in a region 1.5 µm diameter around the endocytosis site (but not including the central ROI) was subtracted. Data from ROIs that were contaminated by other endocytosis events, occurring in close proximity and close in time, were manually excluded from the analysis. It was critical to identify accurately the start and end of each endocytosis event so that individual traces could be averaged. To facilitate this, the rising and falling phases of the intensity trace were fitted with a straight line (60 data points, 3 sec duration), see Figure 3C for example. The intercept of this line with the baseline intensity gave the t_{start} and t_{end} values and event duration ($T_{dur} = t_{end} - t_{start}$) (see Figure 6A). Intensity traces for each given condition were synchronised to the starting point (t_{start}) and averaged (except Cam2-GFP traces which were synchronised using t_{start} measured from simultaneously acquired Cam1-mCherry signal). Similarly, traces were synchronised to their end point (t_{end}) and averaged. The mean duration of the events (T_{dur}) for each condition was then used to reconstruct the mean intensity changes with calculated errors for event amplitude and timing (Table 2). Since the falling and rising phases of most events fitted well to a simple linear equation, the *slope* of the fitted lines was used to estimate the rate of accumulation and dissociation of the fluorescent molecules. As Cam2-GFP remained bound to the endocytic

vesicle, when vesicle scission occurred intensity fell rapidly to zero as the vesicle diffused from the TIRF evanescent field; the time of scission was defined as t_{scis} (Figure 6C). Single particle tracking was performed using, GMimPro (Mashanov & Molloy, 2007) (ASPT module) so that the paths (or trajectories) of individual Myo1 molecules bound to cell membrane could be traced. Trajectories were analysed to yield mean intensities for individual NeonGreen and eGFP labelled proteins, which could be used to estimate the number of fluorescently-tagged molecules associated with each endocytotic event. Intensity-versus-time plots were generated from averages of >30 foci for each protein in each genetic background examined.

Acknowledgements

We thank Professors M. Balasubramanian, I. Hagan, P. Nurse, C. Shimoda and T. Pollard for strains; and Dr Ben Goult for stimulating discussions and comments on the manuscript. This work was supported by the University of Kent and funding from the Biotechnology and Biological Sciences Research Council (BB/J012793/1 & BB/M015130/1), a Royal Society Industry Fellowship to DPM; a CASE industrial bursary from Cairn Research Ltd to KB and by the Francis Crick Institute which receives core funding from Cancer Research UK (FC001119), the UK Medical Research Council (FC001119) and the Wellcome Trust (FC001119) GIM and JEM.

References

Adamek N, Coluccio LM & Geeves MA (2008) Calcium sensitivity of the cross-bridge cycle of Myo1c, the adaptation motor in the inner ear. *Proceedings of the National Academy of Sciences* **105:** 5710–5715

Attanapola SL, Alexander CJ & Mulvihill DP (2009) Ste20-kinase-dependent TEDS-site phosphorylation modulates the dynamic localisation and endocytic function of the fission yeast class I myosin, Myo1. *J. Cell. Sci.* **122:** 3856–3861

Baker K, Kirkham S, Hálová L, Atkin J, Franz-Wachtel M, Cobley D, Krug K, Macek B, Mulvihill DP & Petersen J (2016) TOR complex 2 localises to the cytokinetic actomyosin ring and controls the fidelity of cytokinesis. *J. Cell. Sci.* **129:** 2613–2624

Barker SL, Lee L, Pierce BD, Maldonado-Báez L, Drubin DG & Wendland B (2007) Interaction of the endocytic scaffold protein Pan1 with the type I myosins contributes to the late stages of endocytosis. *Molecular Biology of the Cell* **18:** 2893–2903

Batters C, Arthur CP, Lin A, Porter J, Geeves MA, Milligan RA, Molloy JE & Coluccio LM (2004) Myo1c is designed for the adaptation response in the inner ear. *EMBO J.* **23:** 1433–1440

Bähler J, Wu JQ, Longtine MS, Shah NG, McKenzie A, Steever AB, Wach A, Philippsen P & Pringle JR (1998) Heterologous modules for efficient and versatile PCR-based gene targeting in Schizosaccharomyces pombe. *Yeast* **14:** 943–951

Bement WM & Mooseker MS (1995) TEDS rule: a molecular rationale for differential regulation of myosins by phosphorylation of the heavy chain head. *Cell Motil. Cytoskeleton* **31:** 87–92

Berro J & Pollard TD (2014) Local and global analysis of endocytic patch dynamics in fission yeast using a new 'temporal superresolution' realignment method. *Molecular Biology of the Cell* **25:** 3501–3514

Carbó N, Tarkowski N, Ipiña EP, Dawson SP & Aguilar PS (2016) Sexual pheromone modulates the frequency of cytosolic Ca2+ bursts in Saccharomyces cerevisiae. *Molecular Biology of the Cell* **28:** 501–510

Carpy A, Krug K, Graf S, Koch A, Popic S, Hauf S & Macek B (2014) Absolute proteome and phosphoproteome dynamics during the cell cycle of Schizosaccharomyces pombe (Fission Yeast). *Mol. Cell Proteomics* **13:** 1925–1936

Clos J & Brandau S (1994) pJC20 and pJC40--two high-copy-number vectors for T7 RNA polymerase-dependent expression of recombinant genes in Escherichia coli. *Protein Expression and Purification* **5:** 133–137

Crivici A & Ikura M (1995) Molecular and structural basis of target recognition by calmodulin. *Annu Rev Biophys Biomol Struct* **24:** 85–116

East DA & Mulvihill DP (2011) Regulation and function of the fission yeast myosins. *J. Cell. Sci.* **124:** 1383–1390

Eastwood TA, Baker K, Brooker HR, Frank S & Mulvihill DP (2017) An enhanced recombinant amino-terminal acetylation system and novel in vivohigh-throughput screen for molecules affecting α-synuclein oligomerisation. *FEBS Letters* **106:** 8157–9

Egel R, Willer M, Kjaerulff S, Davey J & Nielsen O (1994) Assessment of pheromone production and response in fission yeast by a halo test of induced sporulation. *Yeast* **10:** 1347–1354

Geiser JR, van Tuinen D, Brockerhoff SE, Neff MM & Davis TN (1991) Can calmodulin function without binding calcium? *Cell* **65:** 949–959

Hayden SM, Wolenski JS & Mooseker MS (1990) Binding of brush border myosin I to phospholipid vesicles. *J. Cell Biol.* **111:** 443–451

Heissler SM & Sellers JR (2016a) Various Themes of Myosin Regulation. *Journal of Molecular Biology* **428:** 1927–1946

Heissler SM & Sellers JR (2016b) Kinetic Adaptations of Myosins for Their Diverse Cellular Functions. *Traffic* **17:** 839–859

Iida H, Yagawa Y & Anraku Y (1990) Essential role for induced Ca2+ influx followed by [Ca2+]i rise in maintaining viability of yeast cells late in the mating pheromone response pathway. A study of [Ca2+]i in single Saccharomyces cerevisiae cells with imaging of fura-2. *J. Biol. Chem.* **265:** 13391–13399

Itadani A, Nakamura T & Shimoda C (2007) Localization of type I myosin and F-actin to the leading edge region of the forespore membrane in Schizosaccharomyces pombe. *Cell Struct. Funct.* **31:** 181–195

Itadani A, Nakamura T, Hirata A & Shimoda C (2010) Schizosaccharomyces pombe Calmodulin, Cam1, Plays a Crucial Role in Sporulation by Recruiting and Stabilizing the Spindle Pole Body Components Responsible for Assembly of the Forespore Membrane. *Eukaryotic Cell* **9:** 1925–1935

Jacinto E, Loewith R, Schmidt A, Lin S, Rüegg MA, Hall A & Hall MN (2004) Mammalian TOR complex 2 controls the actin cytoskeleton and is rapamycin insensitive. *Nat. Cell Biol.* **6:** 1122–1128

Kendrick-Jones J, Smith RC, Craig R & Citi S (1987) Polymerization of vertebrate non-muscle and smooth muscle myosins. *Journal of Molecular Biology* **198:** 241–252

760 Laplante M & Sabatini DM (2012) mTOR signaling in growth control and
761 disease. *Cell* **149:** 274–293

762 Lee S, Comer FI, Sasaki A, McLeod IX, Duong Y, Okumura K, Yates JR III,
763 Parent CA & Firtel RA (2005) TOR Complex 2 Integrates Cell Movement
764 during Chemotaxis and Signal Relay in Dictyostelium. *Molecular Biology*
765 *of the Cell* **16:** 4572–4583

766 Lee WL, Bezanilla M & Pollard TD (2000) Fission yeast myosin-I, Myo1p,
767 stimulates actin assembly by Arp2/3 complex and shares functions with
768 WASp. *The Journal of Cell Biology* **151:** 789–800

769 Lewis JH, Greenberg MJ, Laakso JM, Shuman H & Ostap EM (2012) Calcium
770 regulation of Myosin-I tension sensing. *Biophysical Journal* **102:** 2799–
771 2807

772 Liu L & Parent CA (2011) Review series: TOR kinase complexes and cell
773 migration. *The Journal of Cell Biology* **194:** 815–824

774 Lu Q, Li J, Ye F & Zhang M (2014) Structure of myosin-1c tail bound to
775 calmodulin provides insights into calcium-mediated conformational
776 coupling. *Nat Struct Mol Biol* **22:** 81–88

777 Ma Y, Sugiura R, Koike A, Ebina H, Sio SO & Kuno T (2011) Transient
778 Receptor Potential (TRP) and Cch1-Yam8 Channels Play Key Roles in
779 the Regulation of Cytoplasmic Ca2+ in Fission Yeast. *PLoS ONE* **6:**
780 e22421

781 MacIver FH, Glover DM & Hagan IM (2003) A 'marker switch' approach for
782 targeted mutagenesis of genes in Schizosaccharomyces pombe. *Yeast*
783 **20:** 587–594

784 Marguerat S, Schmidt A, Codlin S, Chen W, Aebersold R & Bähler J (2012)
785 Quantitative analysis of fission yeast transcriptomes and proteomes in
786 proliferating and quiescent cells. *Cell* **151:** 671–683

787 Marks J & Hyams JS (1985) Localization of F-actin through the cell division
788 cycle of Schizosaccharomyces pombe. *European Journal of Cell Biology*
789 **39:** 27–32

790 Mashanov GI & Molloy JE (2007) Automatic detection of single fluorophores
791 in live cells. *Biophysj* **92:** 2199–2211

792 Mashanov GI, Nobles M, Harmer SC, Molloy JE & Tinker A (2010) Direct
793 observation of individual KCNQ1 potassium channels reveals their
794 distinctive diffusive behavior. *J. Biol. Chem.* **285:** 3664–3675

795 Mashanov GI, Tacon D, Knight AE, Peckham M & Molloy JE (2003)
796 Visualizing single molecules inside living cells using total internal reflection
797 fluorescence microscopy. **29:** 142–152

798 Mata J & Bähler J (2006) Global roles of Ste11p, cell type, and pheromone in
799 the control of gene expression during early sexual differentiation in fission
800 yeast. *Proc. Natl. Acad. Sci. U.S.A.* **103:** 15517–15522

801 Mata J, Lyne R, Burns G & Bähler J (2002) The transcriptional program of
802 meiosis and sporulation in fission yeast. *Nat Genet* **32:** 143–147

803 Mentes A, Huehn A, Liu X, Zwolak A, Dominguez R, Shuman H, Ostap EM &
804 Sindelar CV (2018) High-resolution cryo-EM structures of actin-bound
805 myosin states reveal the mechanism of myosin force sensing.
806 *Proceedings of the National Academy of Sciences* **115:** 1292–1297

807 Minc N, Boudaoud A & Chang F (2009) Mechanical forces of fission yeast
808 growth. *Curr. Biol.* **19:** 1096–1101

809 Miseta A, Fu L, Kellermayer R, Buckley J & Bedwell DM (1999) The Golgi
810 apparatus plays a significant role in the maintenance of Ca2+
811 homeostasis in the vps33Delta vacuolar biogenesis mutant of
812 Saccharomyces cerevisiae. *J. Biol. Chem.* **274:** 5939–5947

813 Mitchison JM & Nurse P (1985) Growth in cell length in the fission yeast
814 Schizosaccharomyces pombe. *J. Cell. Sci.* **75:** 357–376

815 Moreno S, Klar A & Nurse P (1991) Molecular genetic analysis of fission yeast
816 Schizosaccharomyces pombe. *Meth. Enzymol.* **194:** 795–823

817 Moser MJ, Flory MR & Davis TN (1997) Calmodulin localizes to the spindle
818 pole body of Schizosaccharomyces pombe and performs an essential
819 function in chromosome segregation. *J. Cell. Sci.* **110 (Pt 15):** 1805–1812

820 Moser MJ, Lee SY, Klevit RE & Davis TN (1995) Ca2+ binding to calmodulin
821 and its role in Schizosaccharomyces pombe as revealed by mutagenesis
822 and NMR spectroscopy. *J. Biol. Chem.* **270:** 20643–20652

823 Mund M, van der Beek JA, Deschamps J, Dmitrieff S, Hoess P, Monster JL,
824 Picco A, Nedelec F, Kaksonen M & Ries J (2018) Systematic Nanoscale
825 Analysis of Endocytosis Links Efficient Vesicle Formation to Patterned
826 Actin Nucleation. *Cell* **174:** 1–13

827 Nguyen AW & Daugherty PS (2005) Evolutionary optimization of fluorescent
828 proteins for intracellular FRET. *Nat Biotechnol* **23:** 355–360

829 O'Connell CB, Tyska MJ & Mooseker MS (2007) Myosin at work: motor
830 adaptations for a variety of cellular functions. *Biochim. Biophys. Acta*
831 **1773:** 615–630

832 Palmer SE, Smaczynska-de Rooij II, Marklew CJ, Allwood EG, Mishra R,
833 Johnson S, Goldberg MW & Ayscough KR (2015) A dynamin-actin
834 interaction is required for vesicle scission during endocytosis in yeast.
835 *Curr. Biol.* **25:** 868–878

836 Pasapera AM, Plotnikov SV, Fischer RS, Case LB, Egelhoff TT & Waterman
837 CM (2015) Rac1-dependent phosphorylation and focal adhesion
838 recruitment of myosin IIA regulates migration and mechanosensing. *Curr.*
839 *Biol.* **25:** 175–186

840 Pearce LR, Komander D & Alessi DR (2010) The nuts and bolts of AGC
841 protein kinases. *Nat Rev Mol Cell Biol* **11:** 9–22

842 Petersen J (2009) TOR signalling regulates mitotic commitment through
843 stress-activated MAPK and Polo kinase in response to nutrient stress.
844 *Biochem. Soc. Trans* **37:** 273–277 Available at:
845 http://eutils.ncbi.nlm.nih.gov/entrez/eutils/elink.fcgi?dbfrom=pubmed&id=1
846 9143645&retmode=ref&cmd=prlinks

847 Petersen J & Nurse P (2007) TOR signalling regulates mitotic commitment
848 through the stress MAP kinase pathway and the Polo and Cdc2 kinases.
849 *Nature Publishing Group* **9:** 1263–1272

850 Picco A, Mund M, Ries J, Nedelec F & Kaksonen M (2015) Visualizing the
851 functional architecture of the endocytic machinery. *eLife* **4:**

852 Redowicz MJ (2001) Regulation of nonmuscle myosins by heavy chain
853 phosphorylation. *J. Muscle Res. Cell. Motil.* **22:** 163–173

854 Rogers SL, Karcher RL, Roland JT, Minin AA, Steffen W & Gelfand VI (1999)
855 Regulation of melanosome movement in the cell cycle by reversible
856 association with myosin V. *The Journal of Cell Biology* **146:** 1265–1276

857 Sammons MR, James ML, Clayton JE, Sladewski TE, Sirotkin V & Lord M
858 (2011) A calmodulin-related light chain from fission yeast that functions
859 with myosin-I and PI 4-kinase. *J. Cell. Sci.* **124:** 2466–2477

860 Sirotkin V, Beltzner CC, Marchand J-B & Pollard TD (2005) Interactions of
861 WASp, myosin-I, and verprolin with Arp2/3 complex during actin patch
862 assembly in fission yeast. *The Journal of Cell Biology* **170:** 637–648

863 Sirotkin V, Berro J, Macmillan K, Zhao L & Pollard TD (2010) Quantitative
864 analysis of the mechanism of endocytic actin patch assembly and
865 disassembly in fission yeast. *Molecular Biology of the Cell* **21:** 2894–2904

866 Suizu T, Tsutsumi H, Kawado A, Suginami K, Imayasu S & Murata K (1995)
867 Calcium ion influx during sporulation in the yeast Saccharomyces
868 cerevisiae. *Can. J. Microbiol.* **41:** 1035–1037

869 Sun Y, Leong NT, Wong T & Drubin DG (2015) A Pan1/End3/Sla1 complex
870 links Arp2/3-mediated actin assembly to sites of clathrin-mediated
871 endocytosis. *Molecular Biology of the Cell* **26:** 3841–3856

872 Sun Y, Martin AC & Drubin DG (2006) Endocytic Internalization in Budding
873 Yeast Requires Coordinated Actin Nucleation and Myosin Motor Activity.
874 *Developmental Cell* **11:** 33–46

875 Takeda T & Yamamoto M (1987) Analysis and in vivo disruption of the gene
876 coding for calmodulin in Schizosaccharomyces pombe. *Proc. Natl. Acad.*
877 *Sci. U.S.A.* **84:** 3580–3584

878 Toya M, Motegi F, Nakano K, Mabuchi I & Yamamoto M (2001) Identification
879 and functional analysis of the gene for type I myosin in fission yeast.
880 *Genes Cells* **6:** 187–199

881 Trybus KM, Gushchin MI, Lui H, Hazelwood L, Krementsova EB, Volkmann N
882 & Hanein D (2007) Effect of calcium on calmodulin bound to the IQ motifs
883 of myosin V. *J. Biol. Chem.* **282:** 23316–23325

884 Tsien RY (1980) New calcium indicators and buffers with high selectivity
885 against magnesium and protons: design, synthesis, and properties of
886 prototype structures. *Biochemistry* **19:** 2396–2404

887 Wilson-Grady JT, Villén J & Gygi SP (2008) Phosphoproteome analysis of
888 fission yeast. *J. Proteome Res.* **7:** 1088–1097

889 Win TZ, Mulvihill DP & Hyams JS (2002) Take five: a myosin class act in
890 fission yeast. *Cell Motil. Cytoskeleton* **51:** 53–56

891

892

Figure Legends

Figure 1. Myo1 serine 742 phosphorylation is TORC2 dependent. (A) Anti-Myo1 western blot of extracts from WT, *gad8*Δ, *ste20*Δ and *myo1.S742A* cells separated using Phos-Tag SDS-PAGE reveals Myo1 is subject to multiple phosphorylation events (*). (B) Sequence alignment of myosin IQ regions shows Myo1^{S742} lies within an AGC consensus sequence, conserved in class I and V myosins. (C) Western blots of extracts from *myo1*$^{+}$ and *myo1-S742A* cells stained with Ponceau S and probed with phospho-specific anti-Myo1^{S742} antibodies demonstrate antigen specificity. (D) Myo1^{S742} is not phosphorylated in *ste20*Δ cells lacking the fission yeast TORC2 regulator Rictor^{Ste20}. (E) Myo1^{S742} is phosphorylated in cells cultured in minimal media containing Glutamic acid (EMMG) but not in EMM2 with an ammonium chloride nitrogen source. (F) WT and *myo1.S742A* cells grown to starvation in EMMG for 72 hrs. In contrast to WT, *myo1.S742A* cells fail to stop growing upon media induced G1 arrest. Scale – 5 µm.

Figure 2. *In vitro* characterisation of interactions between Myo1 and Cam1. (A) Predicted models of the CyPet-Cam1-YPet FRET reporter protein (Cam1-FRET) in the absence (upper panel) and presence (lower panel) of Ca^{2+}. (B) pCa curve plotting Ca^{2+} dependent changes of Cam1-FRET protein conformation (Δ in FRET signal). (C) pCa curve plotting Ca^{2+} dependent changes in IAANS fluorescence of IAANS labelled Cam1-T6C. (D) Transient curves of changes in Quin2 fluorescence brought by Ca^{2+} release from Cam1 (black) and Cam2 (red). (E) Predicted models of the CyPet-Myo1^{IQ12}-YPet FRET reporter protein (Myo1IQ12-FRET) in the absence (upper panel) or presence (lower panel) of Calmodulin binding. (F) Spectra of Myo1^{IQ12}-FRET reporter alone (black line) or with Cam1 in the presence Ca^{2+} (red dotted line) or absence (grey dotted line) of Ca^{2+}. (G) Curves plotting Cam1 dependent changes of FRET donor signal of wild type (black) or S742D phosphomimetic (blue) Myo1^{IQ12}-FRET proteins. (H) Spectra of Myo1^{IQ12}-FRET (black traces) and Myo1$^{IQ12\text{-}S742D}$-FRET (blue traces) in the absence (dashed lines) or presence (lines lines) of Cam1 illustrate differences in conformation of the Myo1 neck region. (I) pCa curve plotting Ca^{2+} dependent changes in acceptor

925 fluorescence of Myo1^{IQ12}-FRET. (J) Curves plotting Cam1 (black) and Cam2
926 (red) dependent changes of FRET donor signal of Myo1-FRET proteins
927 containing single IQ domains (IQ1 – empty shapes; IQ2 – filled shapes).

928 **Figure 3. Myo1 and Cam1 dynamics in wild type and *myo1.S742A* cells.**
929 (A) Maximum projections of 31-z stack widefield images of *mNG.myo1,*
930 *cam1.gfp* and *cam2.gfp* cells (Scales - 5 µm). (B) An example relative intensity
931 trace of a mNeongreen.Myo1 endocytic event. Linear fitting (60 points) was
932 used to find the highest slope for both rising and falling edges. The intercept
933 with zero intensity level was used to calculate T_{begin}, T_{end}, and subsequently the
934 duration of the event. Insert: An arrow shows the location of the endocytosis
935 event (5X5 pixels area). (C) Averaged profile from 50 individual Myo1
936 membrane association events described in (B), synchronised relative to T_{begin}
937 (grey line) and T_{end} (black line). (D) Plot of event duration (sec) against number
938 of Myo1 molecules (fluorescence amplitude). (E) Averaged profile from 52
939 individual Cam1 membrane association events from TIRFM timelapse analysis
940 of *cam1.gfp* cells. (F) Example of fluorescence trace from simultaneously
941 tracking Myo1 and Cam1 membrane binding and disassociation events from
942 TIRFM timelapse analysis of *mNeongreen.myo1 cam1.mCherry* cells. (G)
943 Averaged profiles of combined averages of individual Myo1 (black line and grey
944 s.d.) and Myo1.S742A (grey line) membrane association events from TIRFM
945 timelapse analysis of *mNeongreen.myo1* and *mNeongreen.myo1.S742A* cells
946 respectively. (H) Analysis of mean duration of Myo1 and Cam1 endocytic
947 events in wt and *myo1.S742A* cells from widefield imaging (n > 30). Asterisks
948 denote differences with >99% confidence. (I) Analysis of mean LifeACT and
949 Cam2 signal at endocytic foci in WT and *myo1.S742A* cells (n > 30). No
950 differences observed at 95% level of confidence. All error bars - s.d.

951 **Figure 4. Myo1 S742 is phosphorylated in a cell cycle dependent manner**
952 **to affect polarised growth.** (A) Actin foci periodicity at ends of WT and
953 *myo1.S742A* cells in G2 phase (n>30). Asterisks denote difference with >99%
954 confidence. (B) Graphic highlighting Cdc10 and Cdc25 execution points in
955 relation to cell cycle phases and periods of monopolar / bipolar growth (left).
956 Myo1^{S742} is phosphorylated in *cdc10.v50* arrested G_1 cells, but not in pre-mitotic

G_2 *cdc25.22* arrested cells (right panels). (C) Averaged growth curves from 3 independent experiments of prototroph WT (empty circles) and *myo1.S742A* (grey filled circles) cells cultured in EMMG at 34 ºC. Error bars - s.d. (D) Myosin-1 distribution and cell morphology of prototroph *mNeongreen.myo1*$^+$ and *mNeongreen.myo1.S742A* cells cultured in EMMG at 34 ºC. Asterisks highlight long bent cells. Scale - 10 µm. (E) Calcofluor stained WT and *myo1.S742A* cells. Asterisks highlight long bent cells displaying monopolar growth. Scale - 5 µm. (F) Ratio Sla2-mCherry fluorescence at "new": "old" cell end, averaged from >30 growing mid-log *sla2-mCherry myo1*$^+$ (upper panel) and *sla2-mCherry myo1.S742A* (lower panel) cells. Boxes plot median and quartile for each length measured, lines are plotted from the mean average value at each length measured.

Figure 5. Cam2 associates with internalised endocytic vesicles. (A) Kymographs of GFP labelled foci from maximum projections of 13-z plane timelapse images of *mNeongreen.myo1* (upper panel), *cam1.gfp* (middle panel) and *cam2.gfp* (bottom panel) cells. Myo1 and Cam1 endocytic foci did not move on the membrane (black arrows). Spindle Pole Body (asterisk) and myosin V (white arrow) associated Cam1 are highlighted. In contrast Cam2 foci displayed extensive lateral movements. (B) Kymographs generated from single z-plane timelapse images of single endocytic foci surface during vesicle formation and subsequent internalisation. While Myo1 and Cam1 only associate with the plasma membrane, Cam2, Sla2 and actin are internalised on the vesicle after scission. (C) Kymographs of Cam2 and Sla2 co-internalisation in *sla2.mCherry cam2.gfp* cells. (D) Maximum projection of 31-z slice image of *cam1.mCherry cam2.gfp* cells reveals Cam1 (magenta) and Cam2 (green) colocalise to a subset of endocytic foci. (E-G) Single frames (left panels) and time kymographs (right panels) from maximum projections of 13-z plane timelapse images of *cam1.gfp* (E), *cam2.gfp* (F) and *LifeACT.mCherry* (G) in either *myo1*$^+$ (upper panels) or *myo1*Δ (lower panels) cells show only Cam1 endocytic foci recruitment is dependent upon Myo1. Myo1 is required for internalisation of Cam2-GFP and LifeACT.mCherry labelled foci. Scales - 5 µm.

Figure 6. Cam2 impacts endosome organisation. (A) An example of the

fluorescence trace of Cam2 membrane binding and vesicle internalisation event from TIRFM analysis of *cam2.gfp* cells. An abrupt drop in the fluorescence was marked as "scission time" (grey vertical line). An arrow shows the location of the monitored endocytic event (5X5 pixels area). (B) Averaged profile from 32 individual Cam2 membrane association events (green line) described in (A), together with Cam1-mCherry profile (red) from two-colour TIRFM imaging of *cam1.mCherry cam2.gfp* cells. Events were synchronized relative Cam1 T_{begin} Dashed line denotes mean timing of vesicle scission. (C) Maximum projection of 31-z slice widefield image of a mixture of prototroph *yfp.myo1 sid4.tdTomato* and *yfp.myo1 cam2*Δ cells. (D) Maximum projection of 31-z slice widefield image of a mixture of prototroph *cam1.gfp sid4.tdTomato* and *cam1.gfp cam2*Δ (arrows) cells. (E) Magnification of TIRF heat map of endocytic Cam1 in *cam2*$^{+}$ (upper panel) and *cam2*Δ (lower panel) cells. Squares correspond to regions extending outward from centre of focus. (F) Plot of mean distribution of Cam1 across > 40 endocytic sites in WT and *cam2*Δ cells. (G) Curves plotting Cam2 dependent changes of FRET donor signal of wild type (black) or S742D phosphomimetic (blue) Myo1^{IQ12}-FRET proteins. (H) Spectra of Myo1^{IQ12}-FRET reporter alone (black line), with Cam2 in the presence Ca^{2+} (grey solid line) or absence (grey dotted line) of Ca^{2+}, or with Cam1 in the absence of Ca^{2+} (black dotted line). Scales – 5 µm.

Figure 7. Myo1 S742 phosphorylation regulated Cam1 and Cam2 dynamics during meiosis. (A) Kymographs of Cam2.GFP foci dynamics in *myo1*$^{+}$ (upper panel) and *myo1.S742A* (lower panel) cells. (B) Scheme of consequence of phosphorylation of Myo1 Ser742 (small empty circle) and Ca^{2+} levels upon Cam1 (light grey filled circle) and Cam2 (dark grey filled circle) binding to the IQ1 (solid thick black line) and IQ2 (compound line) motifs of Myo1, and impact on relative orientation of the myosin lever arm (dashed arrow). Highlighted combination of unphosphorylated Myo1^{S742} & Ca^{2+} does not normally occur in wild type cells. (C) Western blots of extracts from G1 arrested *cdc10.v50 myo1*$^{+}$, *cdc10.v50 myo1-S742A* cells, conjugation arrested *fus1*Δ cells or spores, probed with phospho-specific anti-Myo1^{S742} antibodies confirm Myo1S742 remains phosphorylated throughout the sexual cycle. (D) Maximum projection of 13-z slice GFP fluorescence image and transmitted light image

from a timelapse of vegetative (cell 1) and meiotic (cell 2) *gfp-act1* cells. Image from a GFP-act signal. Kymographs in the right panels were generated along the two dotted axes. (E) Histograms of lifetimes of Myo1 (black bars), Cam1 (white bars) and Cam2 (grey bars) foci in vegetative (left panel) and meiotic (right panel) cells. (F) Lifetimes of Myo1, Cam1 and Cam2 foci in WT (white bars) and *myo1.S742A* (black bars) meiotic cells. (G) Micrographs of *myo1.S742A* cell morphology on starvation media. * highlight cells with growth and polarity defects; arrows highlight cells with elongated or abnormally bent shmooing tips; and arrow heads highlight meioses resulting in defective spore formation. Scales – 5 µm.

Figure 8. Model of Myo1 tension dependent interactions at the plasma membrane. (A) Myo1 (green) transiently associates with the plasma membrane. (B) In the presence of early markers of endocytosis (blue) this interaction is stabilised, and Myo1 accumulates to a critical concentration at the endocytic foci (C), whereupon myosin heads associate with growing Arp2/3 (purple) nucleated actin polymers (yellow) attached to the membrane (D), and monitor tension between the actin filament and internalised plasma membrane (E). Upon release of the calmodulin light chain (red), the myosin-1 would its ability to monitor tension and subsequently disengage from the actin polymer and membrane (F).

Supplementary Data Legends

Supplementary Figure 1. Purified proteins used during *in vitro* studies. Coomassie stained SDS-PAGE gel of recombinant proteins expressed and purified during this study. From left to right lanes contain (L) protein standard; (1) Nt-acetylated Cam1; (2) Nt-acetylated Cam1-T6C; (3) Cam1-FRET; (4) Cam2; (5) IQ12 peptide (not used during this study); (6) Myo1IQ12-FRET; and (7) Myo1IQ12S742D-FRET.

Supplementary Figure 2. Relative TIRF profiles. Combined profiles of averages from TIRFM timelapse analysis of Myo1 and Cam1 dynamics in wild type or *myo1.S742A* strains. (A) Myo1 (blue) and Cam1 (red) membrane association in wild type cells. (B) Myo1 membrane association in wild type (blue) and *myo1.S742A* (red) cells. (C) Myo1 (blue) and Cam1 (red) membrane association in *myo1.S742A* cells. (D) Cam1 membrane association in wild type (blue) and *myo1.S742A* (red) cells.

Supplementary Figure 3. Myo1^{S742} phosphorylation fluctuates in a cell cycle dependent manner. A *cdc10.v50* culture was synchronized in G1 by shifting to 36°C for 240 min before returning to 25°C at time 0. Samples of cells were taken every 20 minutes from the release and processed for western blotting to monitor of Myo1^{S742} phosphorylation (A). The membrane was subsequently probed with anti-Myo1 antibodies (B) to monitor total Myo1. Equal loading was monitored by Ponceau staining of the membrane. (C) Densitometry measurements of the bands in these blots are plotted along with the % of cells in the culture with septa.

Supplementary Figure 4. Cam1 and Cam2 do not interact directly. (A) Overlaid OD_{280} spectra were recorded from eluate from a Superdex 75 gel filtration column which had been loaded with either Cam1 (grey line), Cam2 (black line) or Cam1 and Cam2 (red line) under identical 4 mM EGTA buffer conditions. (B) Maximum IAANS fluorescence values (440 nm) of 0.5 μM Cam1-IAANS at a range of pCa values. Black symbols show values of Cam1-IAANS, red symbols show values of Cam1-IAANS with 5 μM Cam2 protein. 2 mM Ca- EGTA buffers were used to give indicated pCa values. pCa_{50} values

calculated from Origin fitting analysis - Hill equation.

Supplementary Figure 5. Multiple labelling strategies for Myo1, Cam1 and Cam2 disrupts normal distribution. Cam1 has increased cytoplasmic signal and reduced signal at endocytic foci in cells expressing both *cam1.gfp* and *mCherry.myo1* (A (GFP-green, mCherry-magenta)) compared to cells expressing *cam1.gfp* alone (B). Similarly, Cam1 has increased cytoplasmic signal and reduced relative signal at endocytic foci in *CFP-myo1 cam1.mCherry* cells (C). (D) Growth curves of prototroph *cam1.gfp* (green) and *cam1.gfp mCherry.myo1* cells cultured in EMMG at 25 ºC. (E) Cam1 (green) localisation is disrupted in *cam1.gfp cam2.mCherry* cells, with less Cam1 on endocytic foci, and localising to the mitotic spindle which is never observed in cells expressing FP labelled Cam1 alone.

Supplementary Movie 1: Timelapse of TIRFM imaged *mNeongreen.myo1* cells showing rapid single molecule interactions of Myo1 at the plasma membrane. Frame Rate: 15 msec / frame.

Supplementary Movie 2: Timelapse of TIRFM imaged *mNeongreen.myo1* cells showing endocytosis associated interactions of Myo1 at the plasma membrane. Frame rate: 50 msec / frame.

Supplementary Movie 3: Timelapse of TIRFM imaged *cam2.gfp* cells showing Cam2 recruiting to endocytic vesicles, to which it remains associated after scission and internalisation of the endosome. Frame rate: 50 msec / frame.

Supplementary Movie 4: Timelapse of TIRFM imaged *cam1.mCherry cam2.gfp* cells showing early recruitment of Cam1 (red) subsequent recruitment of Cam2 (green) to sites of endocytosis. Cam1 disassociates prior to vesicle scission, while Cam2 remains associated with the internalised endosome. Frame rate: 50 msec / frame.

Supplementary Movie 5: Timelapse of maximum projections from 13-z slice widefield images of *mNeongreen.myo1* cells showing typical examples of Myo1 dynamics in vegetative and meiotic cells. Frame rate: 650 msec / frame.

Supplementary Movie 6: Timelapse of maximum projections from 13-z slice widefield images of *cam1.gfp* cells showing typical examples of Cam1 dynamics in vegetative and meiotic cells. Frame rate: 650 msec / frame.

Supplementary Movie 7: Timelapse of maximum projections from 13-z slice widefield images of *cam2.gfp* cells showing typical examples of Cam2 dynamics in vegetative and meiotic cells. Frame rate: 650 msec / frame.

Supplementary Movie 8: Timelapse of maximum projections from 13-z slice widefield images of *gfp.act1* cells showing typical examples of Act1 dynamics in vegetative and meiotic cells. Frame rate: 650 msec / frame.

Supplementary Table 1: Strains used during this study.

Supplementary Table 2: Oligonucleotides used during this study.

Myo1	***mNeonGreen-myo1***	***mNeonGreen-myo1-S742A***	***YFP-myo1 cam2Δ***	-
Whole cell fluorescence (AU)	9,453,813	**0.86** (0.8628)	**0.90** (0.0295)	-
Cell size (μm²)	98.9	**0.84** (0.0863)	**0.95** (0.4542)	-
Maximum intensity (AU)	33,477	**0.92** (0.1446)	**0.62** (0.0001)	-
Number of foci	15.9	**0.82** (0.0203)	**0.84** (0.0261)	-
Average foci volume (μm³)	0.98	**0.98** (0.8595)	**0.64** (0.0001)	-
Total foci volume (μm³)	15.2	**0.75** (0.0020)	**0.53** (0.0001)	-
Total foci fluorescence (AU)	139,712	**0.76** (0.0061)	**0.45** (0.0001)	-
Average foci lifetime (s)	14.0	**10.9** (0.0001)	ND	-
N =	32	30	37	-

Cam1	***cam1-gfp (myo1⁺)***	***cam1-gfp myo1-S742A***	***cam1-gfp cam2Δ***	***cam1-gfp myo1Δ***
Whole cell fluorescence (AU)	61,530,900	**0.89** (0.0197)	**0.97** (0.7145)	**1.14** (0.0733)
Cell size (μm²)	86.1	**0.99** (0.9271)	**1.08** (0.2016)	**1.00** (0.9748)
Maximum intensity (AU)	251,700	**0.82** (0.0563)	**0.72** (0.0001)	**1.41** (0.0001)
Number of foci	14.1	**0.96** (0.6960)	**0.93** (0.3200)	**0.42** (0.0001)
Average foci volume (μm³)	1.12	**0.67** (0.0081)	**0.74** (0.0321)	**1.52** (0.0188)
Total foci volume (μm³)	14.33	**0.68** (0.0004)	**0.78** (0.0703)	**0.56** (0.0001)
Total foci fluorescence (AU)	1,020,350	**0.63** (0.0002)	**0.66** (0.0013)	**0.60** (0.0001)
Average foci lifetime (s)	10.4	9.4 (0.0001)	**13.3** (0.0001)	-
N =	25	15	56	27

Cam2	***cam2-gfp (myo1⁺)***	***cam2-gfp myo1-S742A***	-	***cam2-gfp myo1Δ***
Whole cell fluorescence (AU)	39,259,937	**1.01** (0.8063)	-	**1.48** (0.0001)
Cell size (μm²)	79.3	**0.89** (0.2385)	-	**1.15** (0.3114)
Maximum intensity (AU)	267,547	**0.98** (0.6339)	-	**0.78** (0.0001)
Number of foci	20.8	**0.94** (0.4155)	-	**1.26** (0.0048)
Average foci volume (μm³)	0.82	**1.11** (0.0737)	-	**1.63** (0.0001)
Total foci volume (μm³)	16.53	**1.05** (0.4287)	-	**2.10** (0.0001)
Total foci fluorescence (AU)	859,161	**1.06** (0.3374)	-	**1.82** (0.0001)
N =	20	31	-	17

LifeAct	***LifeAct (myo1⁺)***	***LifeAct myo1-S742A***	***ND***	***LifeAct myo1Δ***
Whole cell fluorescence (AU)	17,116,300	**1.14** (0.0936)	-	**1.15** (0.2851)
Cell size (μm²)	84.5	**1.01** (0.8787)	-	**1.14** (0.1529)
Maximum intensity (AU)	94,671	**1.06** (0.4403)	-	**0.64** (0.016)
Number of foci	19.8	**0.94** (0.5502)	-	**1.22** (0.0147)
Average foci volume (μm³)	0.73	**1.19** (0.0346)	-	**0.95** (0.6822)
Total foci volume (μm³)	13.96	**1.15** (0.1771)	-	**1.14** (0.2759)
Total foci fluorescence (AU)	327,017	**1.18** (0.1832)	-	**1.03** (0.8674)
N =	23	23	-	23

Table 1:
AutoQuantX3 Image analysis data of wide-field fluorescence data of cells. Mutant strains were imaged in mix experiments with wild type cells, analysis for these cells is shown relative to the wild type control cells for each experiment. Statistical significance determined by an unpaired *t-test* is shown in brackets, a statistical significance of $p < 0.05$ is indicated in red.

Protein (*myo1 allele*)	**Duration (SEM)**	**Amplitude (SEM)**	**Rise rate (SEM)**	**Drop rate (SEM)**	**N**
Myo1 (*myo1*$^{+}$)	13.84(0.39)[1,2,3]	2373(155)	536(40.4)	567(43)	50
Cam1 (*myo1*$^{+}$)	10.99(0.21)[1]	4539(292)	1074(83)	1028(69)	52
Myo1 (*myo1.S742A*)	12.28(0.31)[2,4]	2274(128)	536(34)	570(41)	67
Cam1 (*myo1.S742A*)	12.15(0.38)[3,4]	4629(301)	1153(98)	1031(77)	43

Significance differences observed in durations of: [1] Myo1 (wt cells) and Cam1 (wt cells) foci $p<0.0001$; [2] Myo1 (wt cells) and Myo1 (*myo1.S742A* cells) foci $p<0.002$; [3] Myo1 (wt cells) and Cam1 (*myo1.S742A* cells) foci $p<0.0064$.
[4] No significant difference observed between duration of Myo1 (*myo1.S742A* cells) and Cam1 (*myo1.S742A* cells) foci $p<0.79$.

Table 2:
Image analysis data of TIRF data of cells of the indicated genotype.

Figure 1

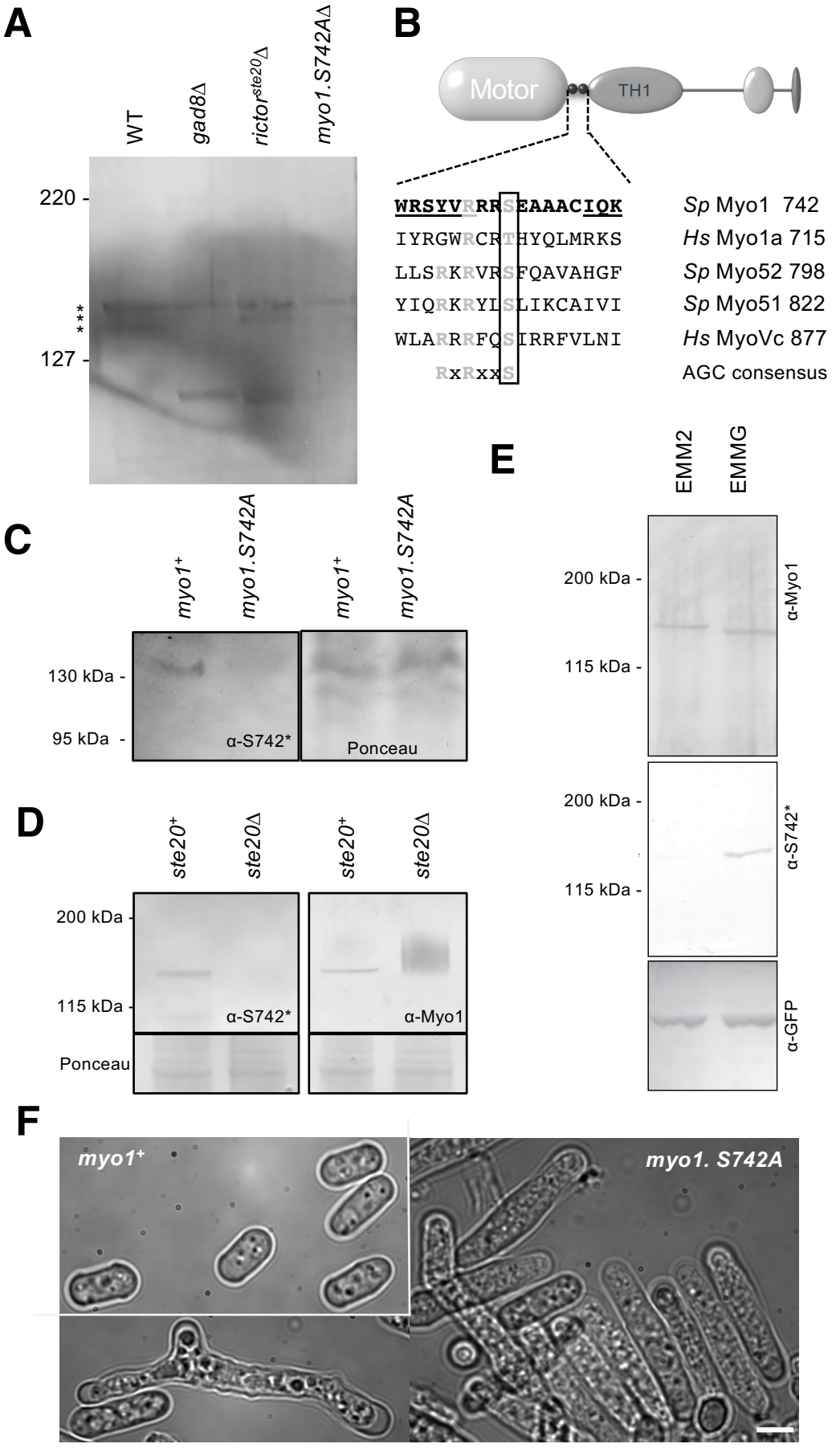
A
WT
gad8Δ
rictor^ste20Δ
myo1.S742AΔ
220 -
***
127 -
B
Motor
TH1
WRSYVRRRSEAAACIQK
IYRGWRCRTHYQLMRKS
LLSRKRVRSFQAVAHGF
YIQRKRYLSLIKCAIVI
WLARRRFQSIRRFVLNI
RxRxxS
Sp Myo1 742
Hs Myo1a 715
Sp Myo52 798
Sp Myo51 822
Hs MyoVc 877
AGC consensus
C
myo1+
myo1.S742A
myo1+
myo1.S742A
130 kDa -
95 kDa -
α-S742*
Ponceau
D
ste20+
ste20Δ
ste20+
ste20Δ
200 kDa -
115 kDa -
α-S742*
α-Myo1
Ponceau
E
EMM2
EMMG
200 kDa -
115 kDa -
α-Myo1
200 kDa -
115 kDa -
α-S742*
α-GFP
F
myo1+
myo1. S742A

Figure 2

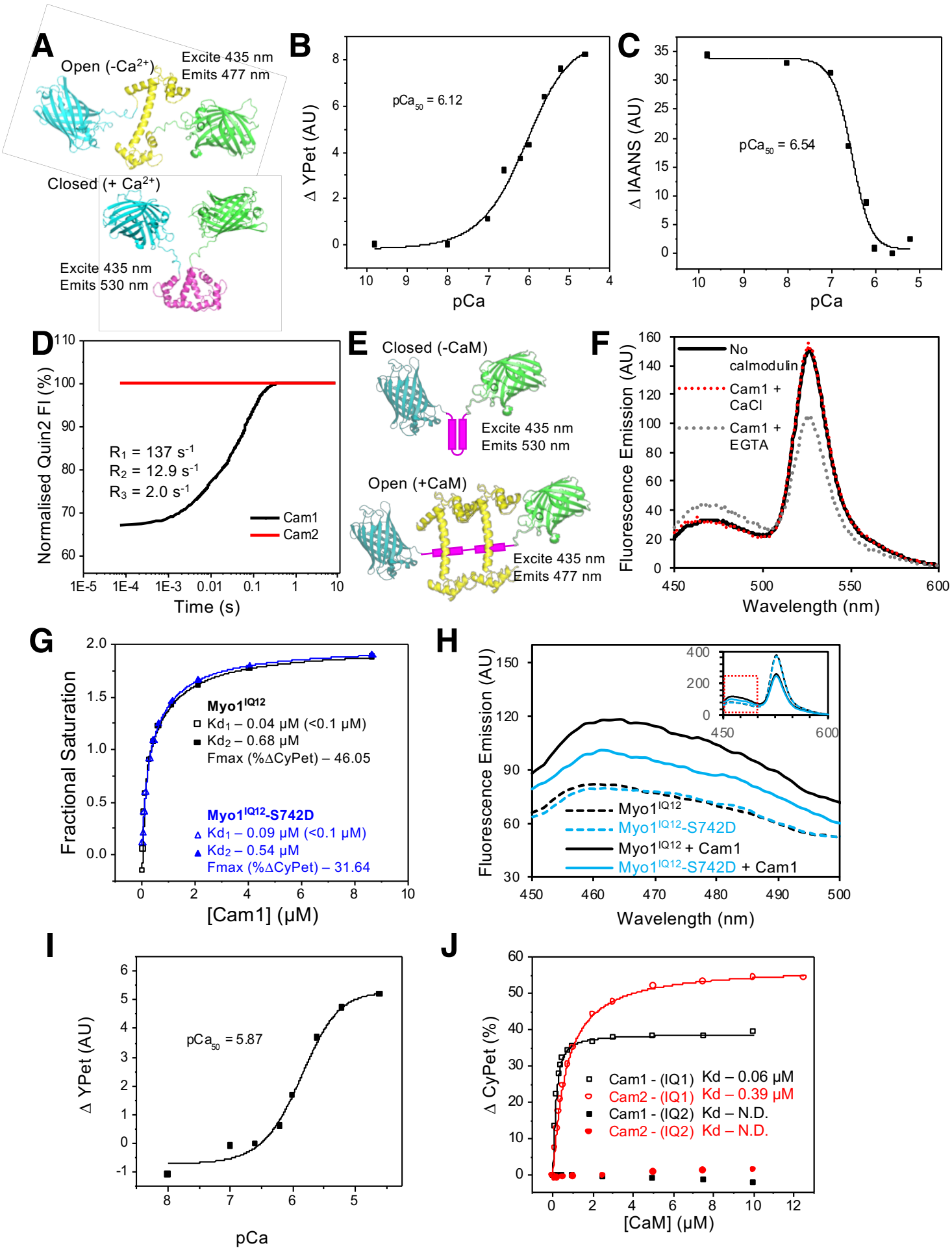
A
Open (-Ca2+)
Excite 435 nm
Emits 477 nm
Closed (+ Ca2+)
Excite 435 nm
Emits 530 nm
B
pCa50 = 6.12
Δ YPet (AU)
pCa
C
pCa50 = 6.54
Δ IAANS (AU)
pCa
D
Normalised Quin2 FI (%)
R1 = 137 s-1
R2 = 12.9 s-1
R3 = 2.0 s-1
Cam1
Cam2
Time (s)
E
Closed (-CaM)
Excite 435 nm
Emits 530 nm
Open (+CaM)
Excite 435 nm
Emits 477 nm
F
No calmodulin
Cam1 + CaCl
Cam1 + EGTA
Fluorescence Emission (AU)
Wavelength (nm)
G
Fractional Saturation
Myo1IQ12
Kd1 – 0.04 μM (<0.1 μM)
Kd2 – 0.68 μM
Fmax (%ΔCyPet) – 46.05
Myo1IQ12-S742D
Kd1 – 0.09 μM (<0.1 μM)
Kd2 – 0.54 μM
Fmax (%ΔCyPet) – 31.64
[Cam1] (μM)
H
Fluorescence Emission (AU)
Myo1IQ12
Myo1IQ12-S742D
Myo1IQ12 + Cam1
Myo1IQ12-S742D + Cam1
Wavelength (nm)
I
pCa50 = 5.87
Δ YPet (AU)
pCa
J
Δ CyPet (%)
Cam1 - (IQ1) Kd – 0.06 μM
Cam2 - (IQ1) Kd – 0.39 μM
Cam1 - (IQ2) Kd – N.D.
Cam2 - (IQ2) Kd – N.D.
[CaM] (μM)

Figure 3

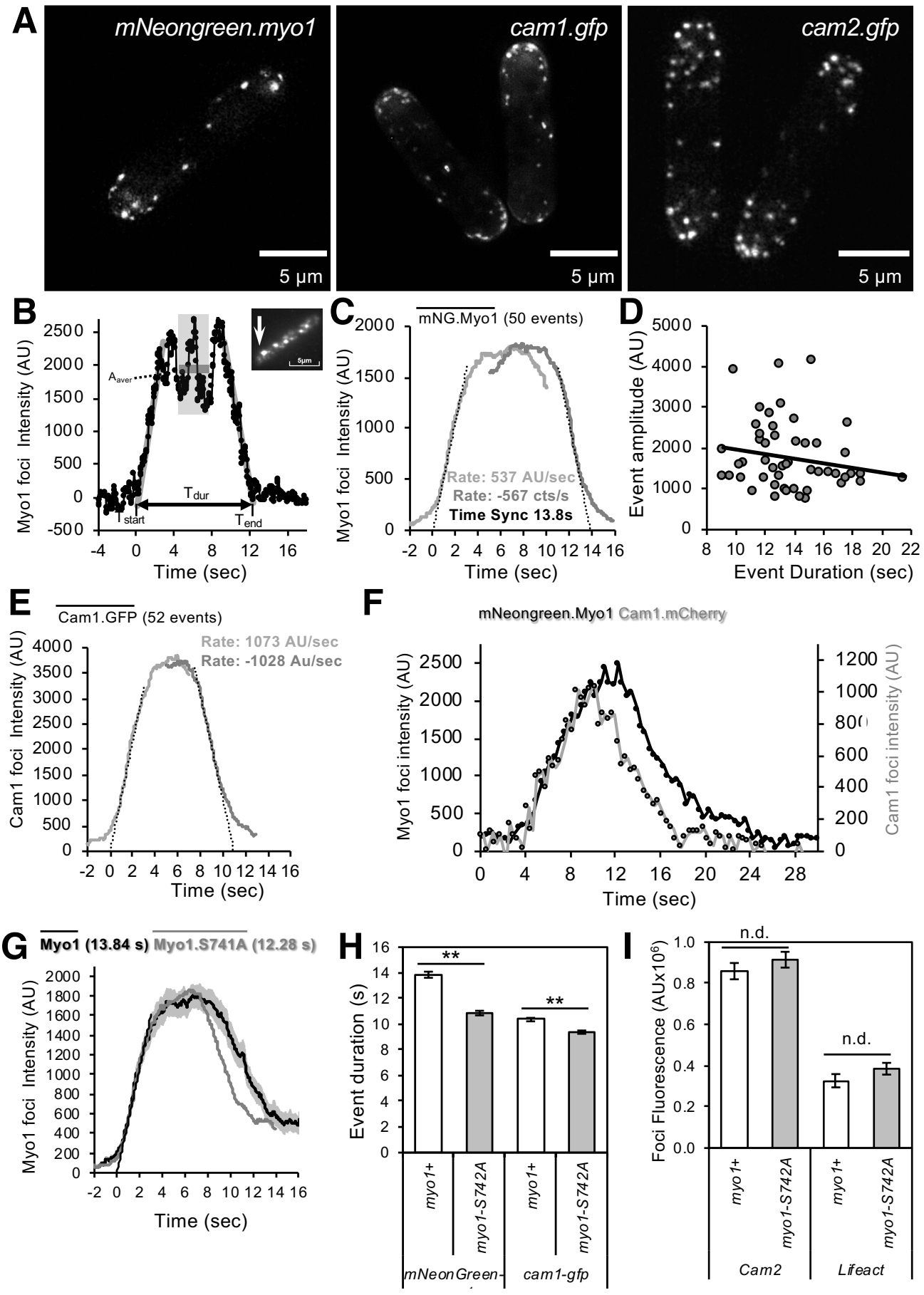
A
mNeongreen.myo1
cam1.gfp
cam2.gfp
5 µm
B
Myo1 foci Intensity (AU)
Time (sec)
A aver
T dur
T start
T end
C
mNG.Myo1 (50 events)
Rate: 537 AU/sec
Rate: -567 cts/s
Time Sync 13.8s
D
Event amplitude (AU)
Event Duration (sec)
E
Cam1.GFP (52 events)
Rate: 1073 AU/sec
Rate: -1028 Au/sec
Cam1 foci Intensity (AU)
F
mNeongreen.Myo1 Cam1.mCherry
Myo1 foci intensity (AU)
Cam1 foci intensity (AU)
G
Myo1 (13.84 s) Myo1.S741A (12.28 s)
H
Event duration (s)
myo1+
myo1-S742A
mNeonGreen-
cam1-gfp
I
Foci Fluorescence (AUx10^6)
n.d.
Cam2
Lifeact

Figure 4

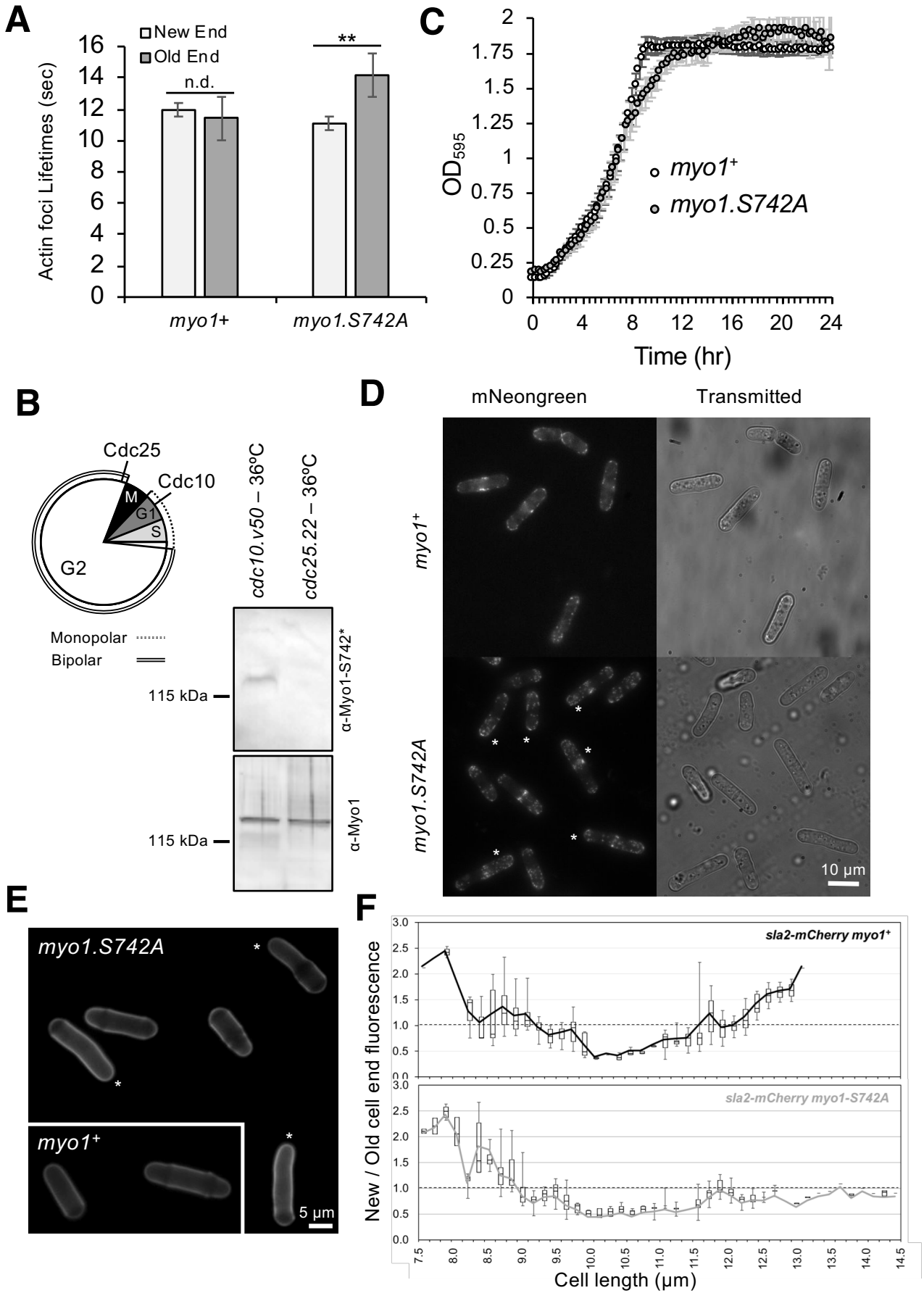
A
New End
Old End
n.d.
**
Actin foci Lifetimes (sec)
myo1+
myo1.S742A
C
OD595
myo1+
myo1.S742A
Time (hr)
B
Cdc25
Cdc10
M
G1
S
G2
Monopolar
Bipolar
cdc10.v50 – 36ºC
cdc25.22 – 36ºC
115 kDa
α-Myo1-S742*
115 kDa
α-Myo1
D
mNeongreen
Transmitted
myo1+
myo1.S742A
10 µm
E
myo1.S742A
myo1+
5 µm
F
sla2-mCherry myo1+
sla2-mCherry myo1-S742A
New / Old cell end fluorescence
Cell length (µm)

Figure 5

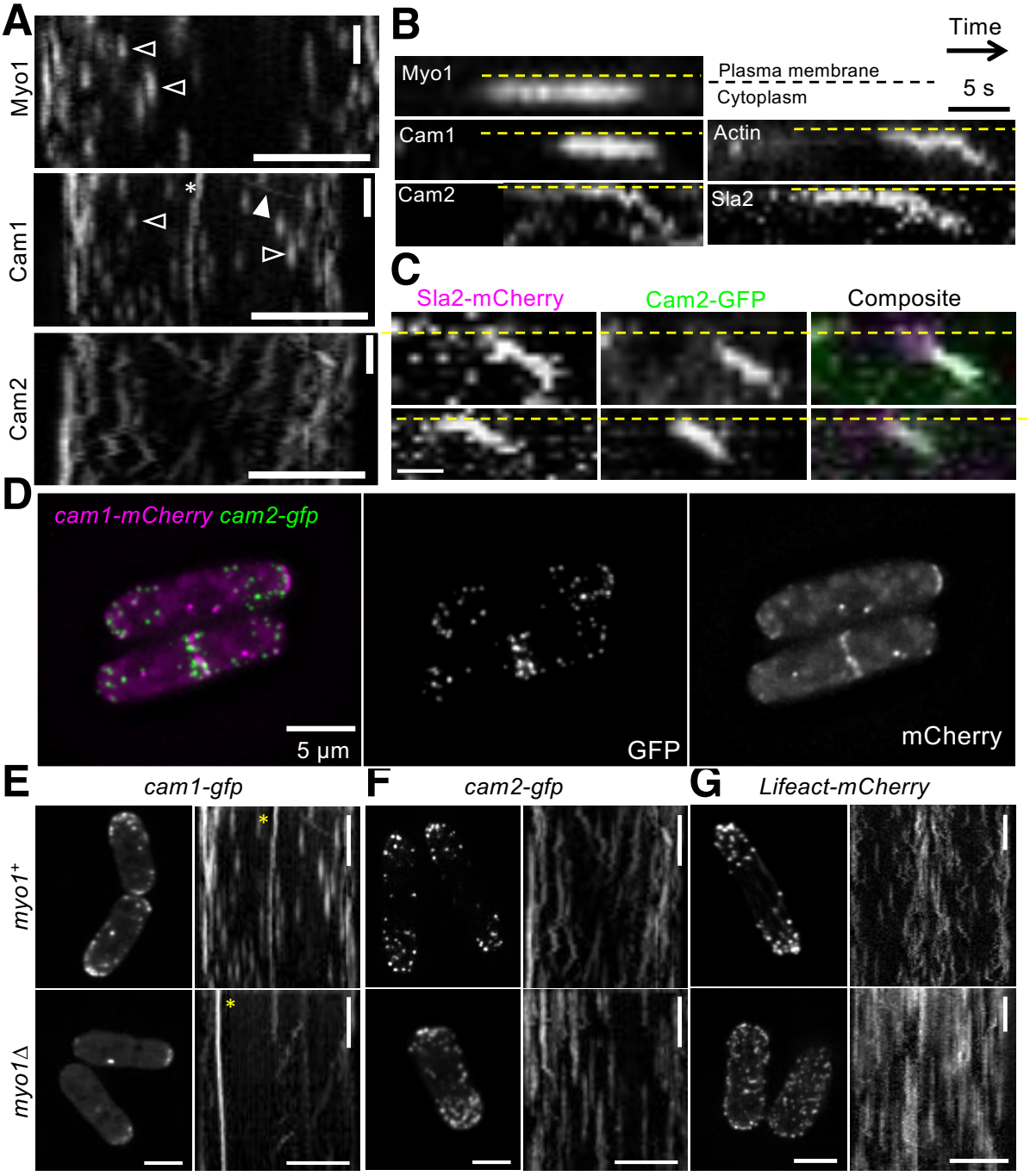
A
Myo1
Cam1
Cam2
B
Time
Myo1
Plasma membrane
Cytoplasm
5 s
Cam1
Actin
Cam2
Sla2
C
Sla2-mCherry
Cam2-GFP
Composite
D
cam1-mCherry cam2-gfp
5 μm
GFP
mCherry
E
cam1-gfp
F
cam2-gfp
G
Lifeact-mCherry
myo1+
myo1Δ

Figure 6

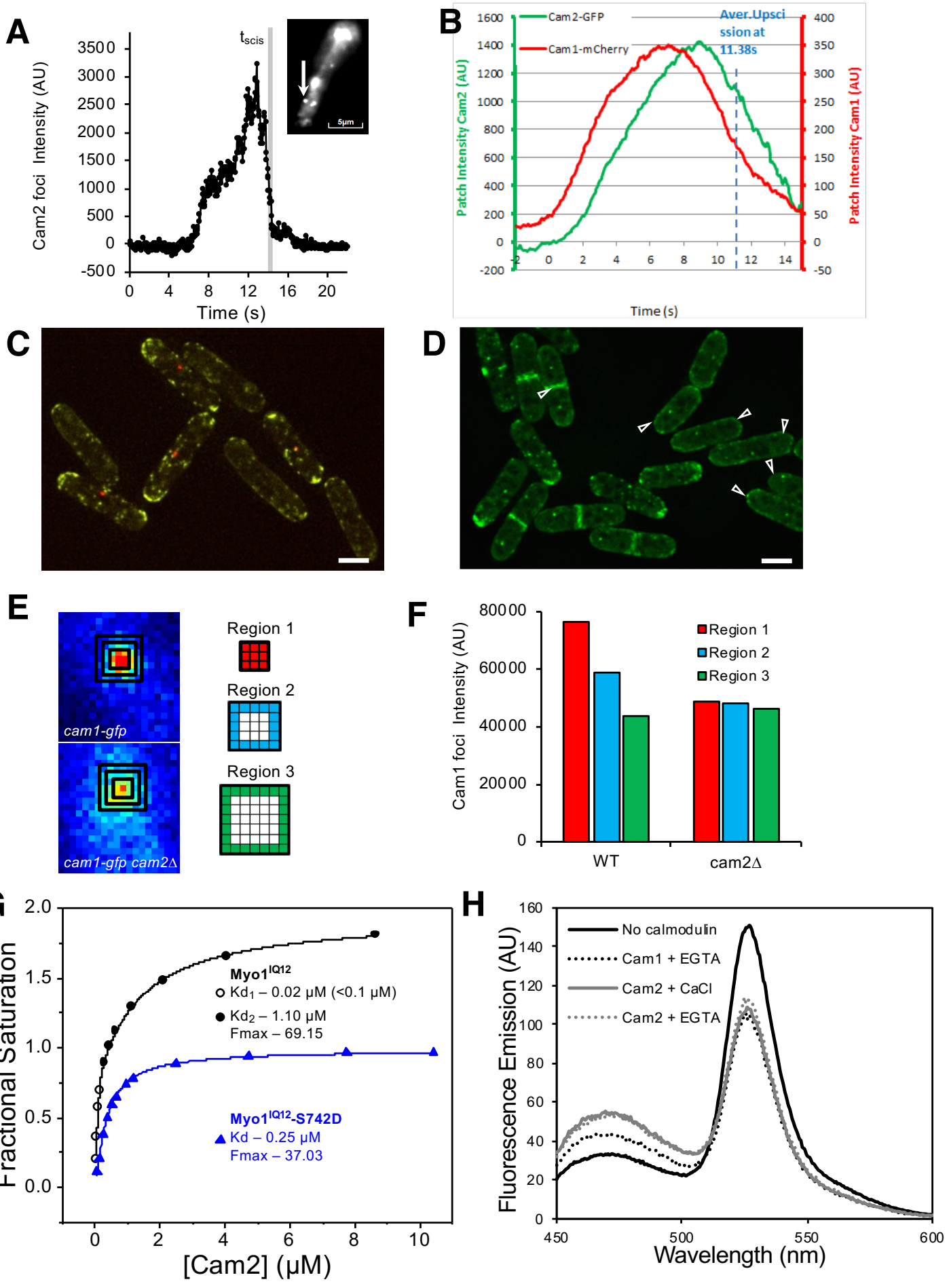
A
Cam2 foci Intensity (AU)
Time (s)
tscis
5µm
B
Cam2-GFP
Cam1-mCherry
Aver.Upscission at 11.38s
Patch Intensity Cam2 (AU)
Patch Intensity Cam1 (AU)
Time (s)
C
D
E
Region 1
Region 2
Region 3
cam1-gfp
cam1-gfp cam2Δ
F
Cam1 foci Intensity (AU)
Region 1
Region 2
Region 3
WT
cam2Δ
G
Fractional Saturation
[Cam2] (µM)
Myo1IQ12
Kd1 – 0.02 µM (<0.1 µM)
Kd2 – 1.10 µM
Fmax – 69.15
Myo1IQ12-S742D
Kd – 0.25 µM
Fmax – 37.03
H
Fluorescence Emission (AU)
Wavelength (nm)
No calmodulin
Cam1 + EGTA
Cam2 + CaCl
Cam2 + EGTA

Figure 7

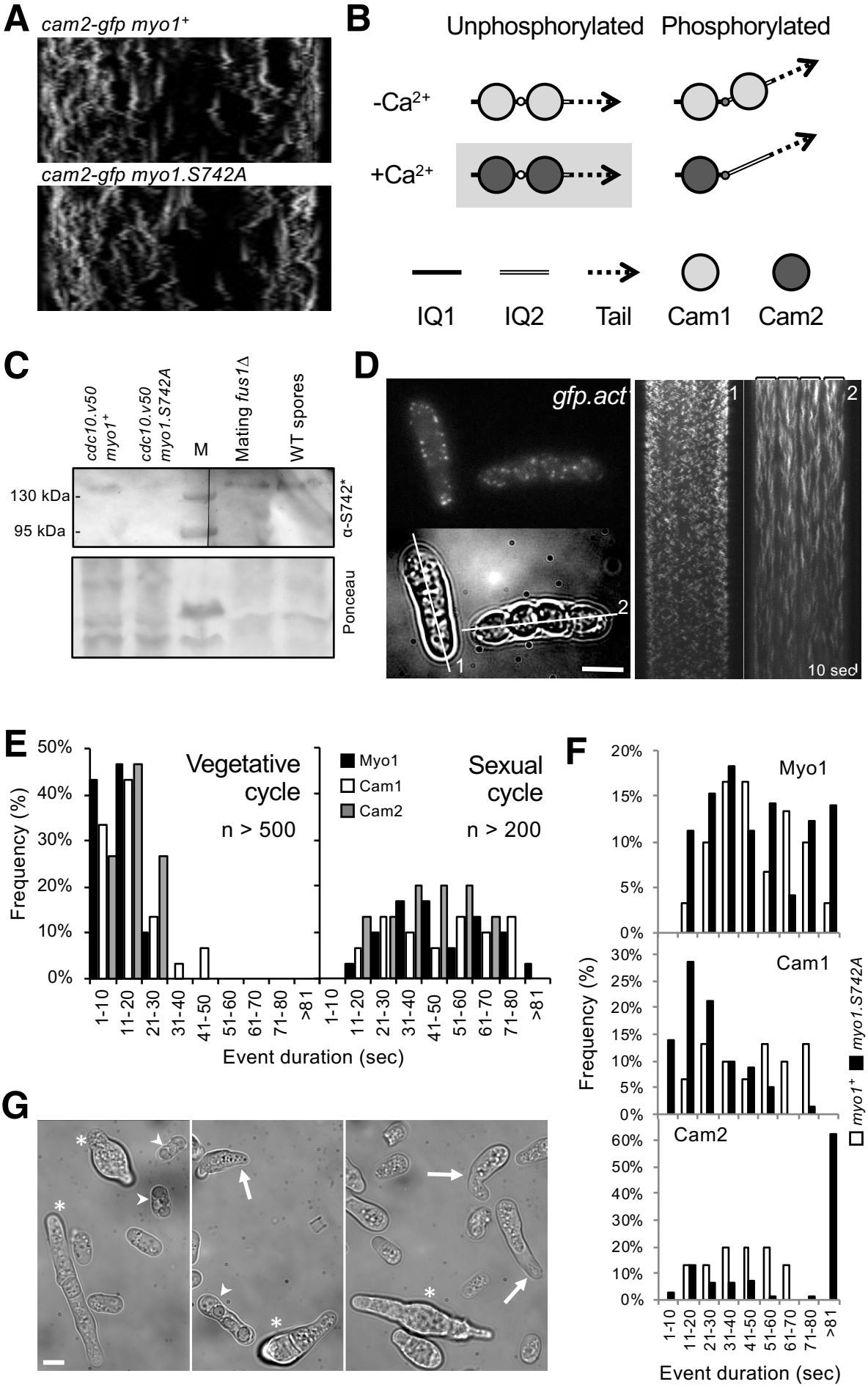
A
cam2-gfp myo1+
cam2-gfp myo1.S742A
B
Unphosphorylated
Phosphorylated
-Ca2+
+Ca2+
IQ1
IQ2
Tail
Cam1
Cam2
C
cdc10.v50 myo1+
cdc10.v50 myo1.S742A
M
Mating fus1Δ
WT spores
130 kDa
95 kDa
α-S742*
Ponceau
D
gfp.act
1
2
10 sec
E
Vegetative cycle
n > 500
Sexual cycle
n > 200
Myo1
Cam1
Cam2
Frequency (%)
Event duration (sec)
F
Myo1
Cam1
Cam2
Frequency (%)
myo1+
myo1.S742A
Event duration (sec)
G

Figure 8

A

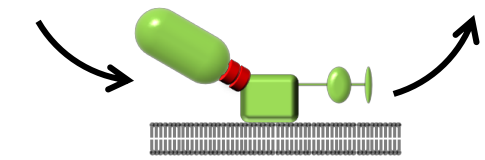

B

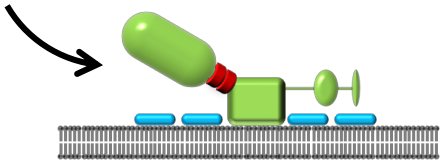

C

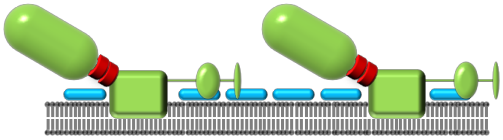

D

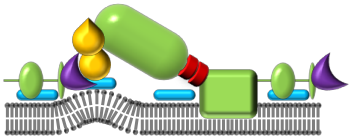

E

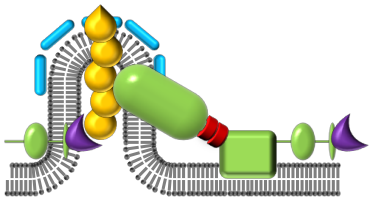

F